Annu. Rev. Earth Planet. Sci. 1990. 18:55–99

CRITICAL TAPER MODEL OF FOLD-AND-THRUST BELTS AND ACCRETIONARY WEDGES

F. A. Dahlen

Department of Geological and Geophysical Sciences,
Princeton University, Princeton, New Jersey 08544

INTRODUCTION

The fold-and-thrust belts and submarine accretionary wedges that lie along compressive plate boundaries are one of the best understood deformational features of the Earth's upper crust. Although there is considerable natural variation among the many fold-and-thrust belts and accretionary wedges that have been recognized and explored, several features appear to be universal. In cross section, fold-and-thrust belts and accretionary wedges occupy a wedge-shaped deformed region overlying a basal detachment or décollement fault; the rocks or sediments beneath this fault show very little deformation. The décollement fault characteristically dips toward the interior of the mountain belt or, in the case of a submarine wedge, toward the island arc; the topography, in contrast, slopes toward the toe or deformation front of the wedge. Deformation within the wedge is generally dominated by imbricate thrust faults verging toward the toe and related fault-bend folding.

Two North American fold-and-thrust belts that exhibit these features are shown in Figure 1. Neither of these two examples is tectonically active today; the southern Canadian fold-and-thrust belt was active during the late Jurassic and Cretaceous (150–100 Ma), whereas the southern Appalachians were deformed during the late Carboniferous to Permian Alleghenian orogeny (300–250 Ma). Figure 2 shows two examples that are currently active: the Taiwan fold-and-thrust belt, produced by the subduction of the Eurasian plate beneath the Philippine Sea plate (Suppe 1981, 1987); and the Barbados accretionary wedge, produced by the sub-

0084–6597/90/0515–0055$02.00

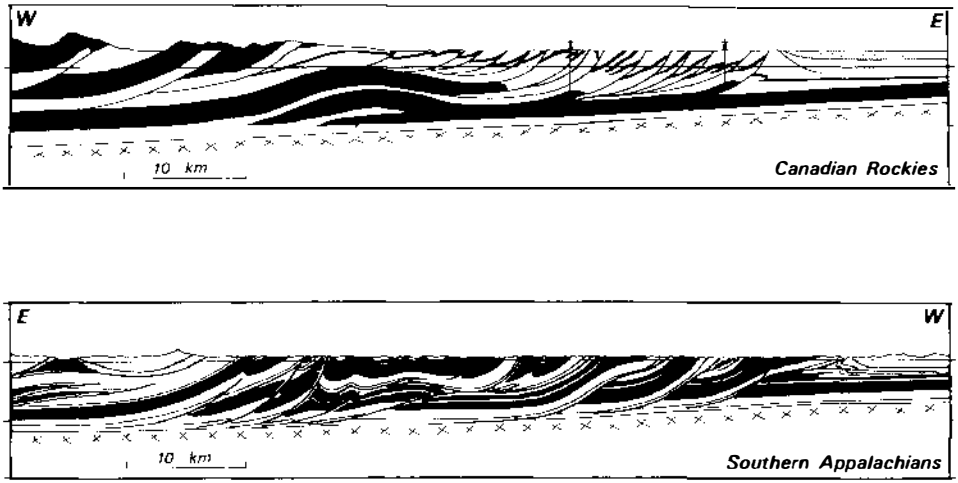

Figure 1 Cross sections of two foreland fold-and-thrust belts. (*Top*) Canadian Rockies (Bally et al 1966). (*Bottom*) Southern Appalachians (Roeder et al 1978). No vertical exaggeration.

duction of the North American plate beneath the Caribbean plate (Westbrook 1975, 1982). These are in a sense two end members of a spectrum, since Taiwan is moderately tapered and rapidly accreting and eroding, whereas Barbados is narrowly tapered, slowly accreting, and noneroding. Evidence that thin-skinned folding and thrusting was a common phenomenon much farther back in the Earth's history is shown in Figure 3. This cross section of the 1900-Ma Asiak fold-and-thrust belt in the northwest Canadian shield was constructed without benefit of seismic or drilling data, by downplunge projection of geological maps (Hoffman et al 1988). Every structural detail has been trod upon by a field geologist's boot.

Mechanically, a fold-and-thrust belt or accretionary wedge is analogous to a wedge of sand in front of a moving bulldozer. The sand, rock, or sediment deforms until it develops a constant critical taper; if no fresh material is encountered at the toe, the wedge then slides stably without further deformation as it is pushed. The magnitude of the critical taper is governed by the relative magnitudes of the frictional resistance along the base and the compressive strength of the wedge material. An increase in the sliding resistance increases the critical taper, since it is the drag on the base that is fundamentally responsible for the deformation. An increase in the wedge strength, on the other hand, decreases the critical taper, since a stronger wedge can be thinner and still slide stably over a rough base

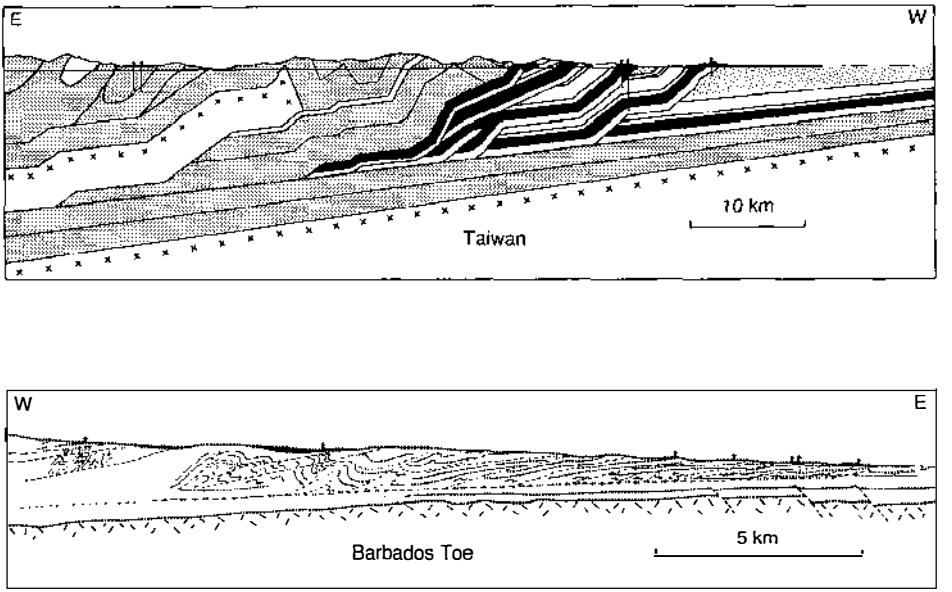

Figure 2 (*Top*) Cross section of the active fold-and-thrust belt in northern Taiwan (Suppe 1980). (*Bottom*) Cross section of the frontal region of the Barbados accretionary wedge near 15°30′N latitude (Behrmann et al 1988). Locations of Deep Sea Drilling Project and Ocean Drilling Program drill sites are indicated. No vertical exaggeration.

without deforming. The state of stress within a critically tapered wedge in the upper crust is everywhere on the verge of Coulomb failure, since the taper is attained by a process of continued brittle frictional deformation.

This paper describes an idealized mechanical model of a fold-and-thrust belt or accretionary wedge, based on this bulldozer analogy. The first analyses in this spirit were developed by Elliott (1976) and Chapple (1978); their ideas were later refined and extended to incorporate a brittle frictional rheology by Davis et al (1983). For the most part, we consider only the simplest possible version of the model, which ignores cohesion and assumes that the material properties within the wedge and on the basal décollement fault are spatially uniform (Dahlen 1984). A more general approximate analysis is, however, also discussed. Special attention is paid to the effects of pore fluids, since elevated pore-fluid pressures play such an important role in the mechanics of overthrust faulting (Hubbert & Rubey 1959). Pore-fluid pressure effects were accounted for by Davis et al (1983) and Dahlen (1984); however, a significant point was not spelled out clearly, and that is rectified here.

Figure 3 Cross section of the Asiak fold-and-thrust belt, eastern Wopmay orogen, in the northwest Canadian shield (Hoffman et al 1988). No vertical exaggeration.

MECHANICS OF A BULLDOZER WEDGE

Kinematics

We begin with a simplified discussion of the mechanics of a bulldozer wedge. Suppose a rigid hillside of slope β is covered with a uniform layer of dry sand of thickness h (Figure 4). If at time $t = 0$ a bulldozer begins moving uphill at a uniform velocity V, scraping up sand, a critically tapered wedge of deformed sand will form in front of the moving bulldozer. Let α denote the surface slope of this deformed wedge; the critical taper is the angle at the toe, $\alpha+\beta$. The mass flux per unit length along strike into the toe of the wedge is ρhV, where ρ is the sand density. We ignore compaction and assume that ρ is a constant. The growth of the wedge with time is described by the mass conservation law

$$\frac{\mathrm{d}}{\mathrm{d}t}\left[\frac{1}{2}\rho W^2 \tan(\alpha+\beta)\right] = \rho hV, \tag{1}$$

where W is the wedge width. Since $\alpha+\beta$ does not change with time, Equation (1) reduces to

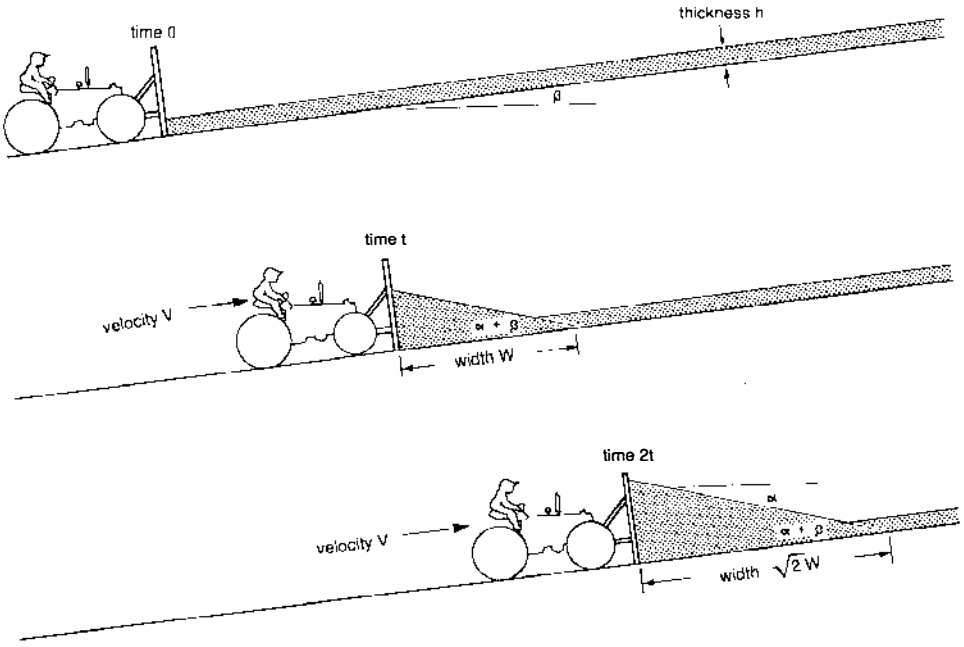

Figure 4 Cartoon depicting the self-similar growth of a bulldozer wedge.

$$W\frac{dW}{dt} = \frac{hV}{\tan(\alpha+\beta)}. \tag{2}$$

This has the solution

$$W = \left[\frac{2hVt}{\tan(\alpha+\beta)}\right]^{1/2} \approx \left[\frac{2hVt}{\alpha+\beta}\right]^{1/2}. \tag{3}$$

The final approximation is valid for a wedge of narrow taper, $\alpha+\beta \ll 1$, where α and β are measured in radians. Because the critical taper is governed only by the unvarying strength of the sand and the basal friction, both the width and the height of a bulldozer wedge grow like $t^{1/2}$. The growth is self-similar in the sense that the wedge at time $2t$ is indistinguishable from the wedge at time t, magnified $2^{1/2}$ times.

An eroding wedge will attain a dynamic steady state when the accretionary influx rate of fresh material into the toe is balanced by the erosive efflux (Figure 5). The steady-state width of a uniformly eroding wedge is given by the flux balance condition

$$\dot{e}W\sec(\alpha+\beta) \approx \dot{e}W = hV, \tag{4}$$

where $\dot{e}$ is the rate of erosion. A steady-state wedge must continually deform both to accommodate the influx of fresh material into its toe and to maintain its critical taper against erosion.

Critical Taper

Let (x, z) be a system of Cartesian coordinates with x aligned along the top of the wedge and z pointing down (Figure 6). To determine the critical

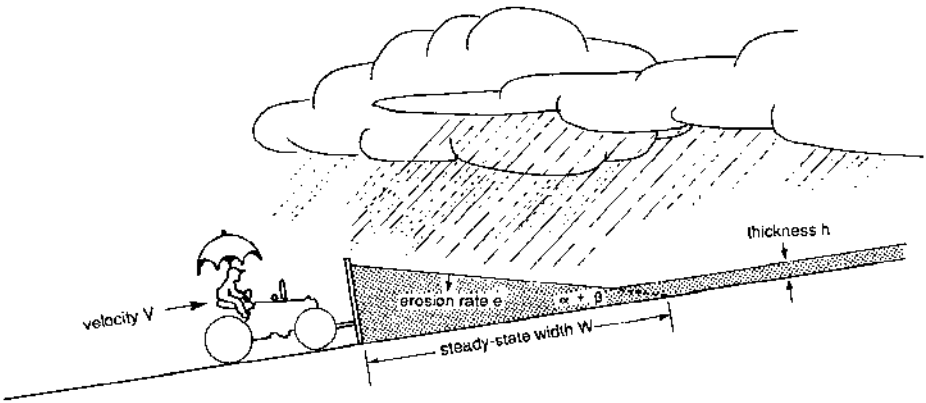

Figure 5 An eroding wedge attains a dynamic steady-state width given by $\dot{e}W = hV$.

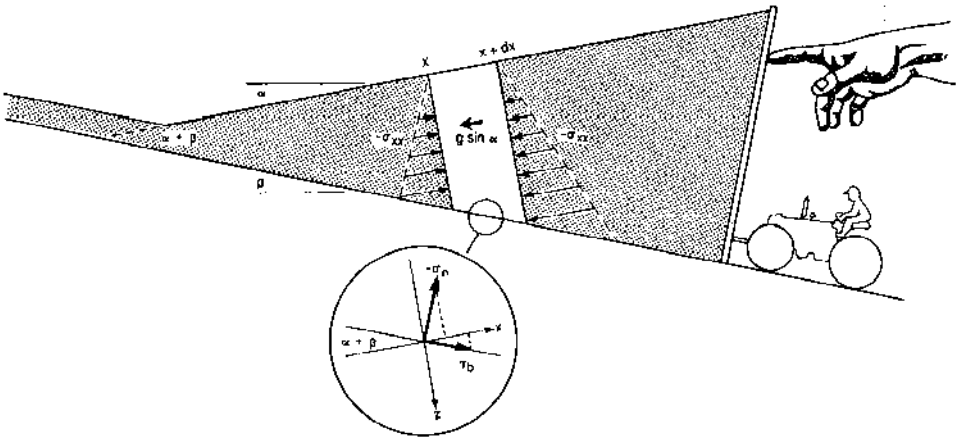

Figure 6 Schematic diagram illustrating the horizontal balance of forces on an element of a bulldozer wedge.

taper, we consider the balance of forces on an infinitesimal segment of the wedge lying between x and $x+\mathrm{d}x$; it suffices to consider the forces acting in the $\pm x$ direction. First, there is a gravitational body force whose x component, per unit length along strike, is

$$F_g = -\rho g H \sin\alpha \, \mathrm{d}x, \tag{5}$$

where g is the acceleration of gravity, and H is the local wedge thickness. Second, there is the net force exerted by the compressive tractions σ_{xx} acting on the sidewalls at x and $x+\mathrm{d}x$; if we adopt the convention that a compressive stress is negative, this force is given by

$$F_s = \int_0^H [\sigma_{xx}(x+\mathrm{d}x, z) - \sigma_{xx}(x, z)]\,\mathrm{d}z. \tag{6}$$

Third, and finally, there is the surface force exerted on the base; this is given in terms of the local shear and normal tractions τ_b and σ_n by

$$F_b = [\tau_b \cos(\alpha+\beta) - \sigma_n \sin(\alpha+\beta)]\,\mathrm{d}x. \tag{7}$$

We assume that the base is governed by a frictional sliding condition

$$\tau_b = -\mu_b \sigma_n, \tag{8}$$

where μ_b is the coefficient of basal friction; the basal traction then reduces to

$$F_b = -\sigma_n[\mu_b \cos(\alpha+\beta)+\sin(\alpha+\beta)]\,dx. \tag{9}$$

The balance condition is

$$F_g+F_s+F_b=0. \tag{10}$$

The first two forces, F_g and F_s, act in the $-x$ direction, whereas F_b acts in the $+x$ direction. Upon taking the limit as $dx \to 0$, Equation (10) reduces to the exact result

$$-\rho g H \sin\alpha - \sigma_n[\mu_b \cos(\alpha+\beta)+\sin(\alpha+\beta)]+\frac{d}{dx}\int_0^H \sigma_{xx}\,dz = 0. \tag{11}$$

For $\alpha \ll 1$ and $\beta \ll 1$ we employ the approximations $\sin\alpha \approx \alpha$, $\sin(\alpha+\beta) \approx \alpha+\beta$, $\cos(\alpha+\beta) \approx 1$, and $\sigma_n \approx -\rho g H$. This reduces Equation (11) to

$$\rho g H(\beta+\mu_b)+\frac{d}{dx}\int_0^H \sigma_{xx}\,dz \approx 0. \tag{12}$$

The failure criterion for noncohesive dry sand can be written in the form

$$\frac{\sigma_1}{\sigma_3}=\frac{1+\sin\phi}{1-\sin\phi}. \tag{13}$$

Here σ_1 and σ_3 are the greatest and least principal compressive stresses, respectively, and ϕ is the angle of internal friction (Jaeger & Cook 1969, pp. 87–91). In a narrow taper ($\alpha \ll 1$ and $\beta \ll 1$), the principal stresses are approximately horizontal and vertical, that is

$$\sigma_{zz} \approx \sigma_3 \approx -\rho g z, \tag{14a}$$

$$\sigma_{xx} \approx \sigma_1 \approx -\left(\frac{1+\sin\phi}{1-\sin\phi}\right)\rho g z. \tag{14b}$$

The sidewall traction term in Equation (12) reduces in this approximation to

$$\frac{d}{dx}\int_0^H \sigma_{xx}\,dz \approx -\left(\frac{1+\sin\phi}{1-\sin\phi}\right)\rho g H(\alpha+\beta), \tag{15}$$

where we have used the relation $dH/dx \approx \alpha+\beta$. Upon inserting Equation (15) into (12), we obtain the approximate critical taper equation for a dry sand wedge in front of a bulldozer:

$$\alpha+\beta \approx \left(\frac{1-\sin\phi}{1+\sin\phi}\right)(\beta+\mu_b). \tag{16}$$

Discussion

Equation (16) shows that the critical taper $\alpha+\beta$ is increased by an increase in the coefficient of basal friction μ_b, whereas it is decreased by an increase in the internal friction angle ϕ. For $\phi = 30°$, a typical value for dry sand, the critical surface slope is given by $\alpha \approx \frac{1}{3}(\mu_b - 2\beta)$. Idle conjecture might have led to the conclusion that the surface slope α of a bulldozer wedge is at the angle of repose ($\phi = 30°$), but in fact the state of stress and therefore the slope are completely different.

Equation (12) describes the quasi-static balance of forces in any thin-skinned wedge being pushed up a frictional incline. To make use of this result, it is necessary to relate the horizontal compressive stress σ_{xx} to the stress due to the lithostatic overburden, $\sigma_{zz} \approx -\rho g z$. In a critically tapered wedge, σ_{xx} is related to σ_{zz} by the Coulomb failure law:

$$\sigma_{xx}^{\text{failure}} \approx -\left(\frac{1+\sin\phi}{1-\sin\phi}\right)\rho g z. \tag{17}$$

A thinner (subcritical) wedge being pushed up the same incline has σ_{xx} greater than $\sigma_{xx}^{\text{failure}}$; such a wedge fails and increases its taper until it becomes critical. A thicker (supercritical) wedge has σ_{xx} less than $\sigma_{xx}^{\text{failure}}$, so it can be pushed up the incline without deforming if no fresh material is encountered at the toe. In determining the critical taper, we have solved a stability problem, since a subcritical wedge is unstable, and a supercritical wedge stable, when pushed up the same incline. Any wedge that is formed by offscraping and the progressive failure of the material within it should have $\sigma_{xx} \approx \sigma_{xx}^{\text{failure}}$—this is the essential premise of the critical taper model.

BALANCE OF FORCES IN A POROUS MEDIUM

The brittle frictional strength of rocks in the upper crust is significantly affected by the presence of water and other interstitial pore fluids. The important role played by pore-fluid pressure in overthrust faulting was first pointed out in the classic and influential paper of Hubbert & Rubey (1959). Their discussion is extremely lucid and well worth reading over 30 years later. One aspect that led to some controversy following the original publication is their calculation of the force exerted by a pore fluid on a porous solid (Laubscher 1960, Moore 1961, Hubbert & Rubey 1960, 1961). This is a subtle issue that has been overlooked in previous critical taper analyses, and we address it in some detail here.

Microscopic Equations

We model a porous medium as a solid skeleton or matrix whose pore spaces are completely filled by a homogeneous incompressible fluid of constant density ρ_f and constant viscosity ν. The density $\rho_s(\mathbf{x})$ of the solid is regarded as a function of position $\mathbf{x}$ to allow for density variations from grain to grain. We denote the stress tensors within the fluid and solid, respectively, by $\boldsymbol{\sigma}_f(\mathbf{x})$ and $\boldsymbol{\sigma}_s(\mathbf{x})$. The fluid stress is related to the fluid velocity $\mathbf{u}(\mathbf{x})$ within the pore spaces by the Newtonian constitutive equation

$$\boldsymbol{\sigma}_f = -p_f\mathbf{I} + \nu[\nabla_x\mathbf{u} + (\nabla_x\mathbf{u})^T], \tag{18}$$

where $\mathbf{I}$ is the identity tensor, and T denotes the transpose. We affix a subscript $\mathbf{x}$ to the gradient operator ∇ to emphasize that it describes the change in a quantity due to a change in the microscopic position variable $\mathbf{x}$. The quantity $p_f(\mathbf{x})$ is the microscopic pore-fluid pressure. The pointwise momentum balance equations within the solid and fluid are

$$\nabla_x \cdot \boldsymbol{\sigma}_s + \rho_s\mathbf{g} = \mathbf{0}, \tag{19a}$$

$$\nabla_x \cdot \boldsymbol{\sigma}_f + \rho_f\mathbf{g} = \mathbf{0}, \tag{19b}$$

where $\mathbf{g}$ is the acceleration of gravity. Inertial forces $\rho_f(\partial_t\mathbf{u} + \mathbf{u}\cdot\nabla_x\mathbf{u})$ have been ignored in writing Equation (19b), since the flow is assumed to be in the creeping (low-Reynolds-number) regime. Equations (18) and (19b) together can be written in the form

$$-\nabla_x p_f + \nu\nabla_x^2\mathbf{u} + \rho_f\mathbf{g} = \mathbf{0}. \tag{20}$$

This is the well-known Navier-Stokes equation, with inertial forces ignored (Batchelor 1967, pp. 216–17).

Volume Averaging

Equations (19) and (20) are far too complicated to use directly because of the rapid variation from fluid to solid on the microscopic scale. We seek instead a system of averaged equations that are valid on the macroscopic scale. The procedure of averaging a system of microscopic equations to obtain a simpler system of macroscopic equations is a common one; in electromagnetism it is the basis for extending Maxwell's equations to dielectric and magnetic materials (Jackson 1962, pp. 103–8, 150–54). Averaging has been used to obtain the macroscopic equations governing a porous medium by several authors, including Whitaker (1969), Saffman (1971), Slattery (1972, pp. 191–215), Gray & O'Neill (1976), and Lehner (1979).

Consider an averaging volume V centered on an arbitrary point $\bar{\mathbf{x}}$, as

shown in Figure 7 (*left*). Let V_s and V_f be the volumes within V occupied by the solid and fluid, respectively. The porosity $\eta(\bar{\mathbf{x}})$ is defined by

$$\eta = V_f/V. \tag{21}$$

In order for the averaging to be meaningful, the size of the averaging volume must be much smaller than a typical macroscopic scale length but large enough to average over many solid grains and many pore spaces. In this limit, it is immaterial whether we regard $\bar{\mathbf{x}}$ as the centroid of the whole volume V, or as the centroid of the solid matter contained within V_s, or as the centroid of the pore space V_f. We regard the porosity η and all other macroscopic variables as continuous functions of the macroscopic position variable $\bar{\mathbf{x}}$.

Upon averaging Equation (19a) over V_s and Equation (19b) over V_f, we obtain

$$\frac{1}{V_s}\int_{V_s} \nabla_{\mathbf{x}} \cdot \boldsymbol{\sigma}_s \, dV + \bar{\rho}_s \mathbf{g} = \mathbf{0}, \tag{22a}$$

$$\frac{1}{V_f}\int_{V_f} \nabla_{\mathbf{x}} \cdot \boldsymbol{\sigma}_f \, dV + \rho_f \mathbf{g} = \mathbf{0}. \tag{22b}$$

The quantity $\bar{\rho}_s(\bar{\mathbf{x}})$ is the macroscopic solid density, given by

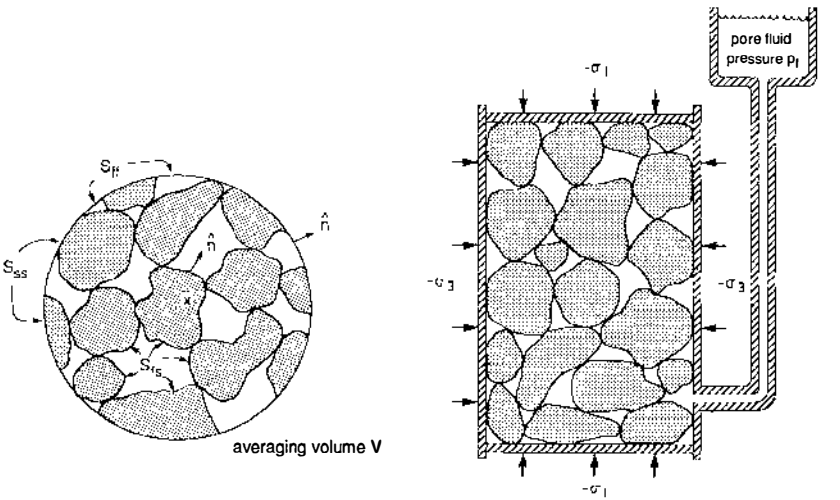

Figure 7 (*Left*) Schematic diagram of a portion of a porous medium within a representative averaging volume V. The interface between the solid grains and the pore spaces is denoted by S_{fs}. (*Right*) Schematic diagram of a typical rock-mechanics laboratory friction or fracture experiment.

$$\bar{\rho}_s = \frac{1}{V_s}\int_{V_s} \rho_s \, dV. \tag{23}$$

Equations (22) can alternatively be written in the form

$$\frac{1}{V}\int_{V_s} \nabla_{\mathbf{x}} \cdot \boldsymbol{\sigma}_s \, dV + (1-\eta)\bar{\rho}_s \mathbf{g} = \mathbf{0}, \tag{24a}$$

$$\frac{1}{V}\int_{V_f} \nabla_{\mathbf{x}} \cdot \boldsymbol{\sigma}_f \, dV + \eta \rho_f \mathbf{g} = \mathbf{0}. \tag{24b}$$

We define the macroscopic solid and fluid stresses $\bar{\boldsymbol{\sigma}}_s(\bar{\mathbf{x}})$ and $\bar{\boldsymbol{\sigma}}_f(\bar{\mathbf{x}}) = -\bar{p}_f(\bar{\mathbf{x}})\mathbf{I}$ by

$$\bar{\boldsymbol{\sigma}}_s = \frac{1}{V_s}\int_{V_s} \boldsymbol{\sigma}_s \, dV, \tag{25a}$$

$$\bar{\boldsymbol{\sigma}}_f = -\bar{p}_f \mathbf{I} = \frac{1}{V_f}\int_{V_f} \boldsymbol{\sigma}_f \, dV. \tag{25b}$$

Note that the macroscopic fluid stress is considered to be isotropic, even though viscous shear stresses may be comparable to the dynamical pressure fluctuations on the microscopic scale.

The boundary of the averaging volume V has portions S_{ss} in the solid grains and portions S_{ff} in the fluid-filled pore spaces, as shown in Figure 7 (*left*). We denote the fluid-solid interface situated within the volume V by S_{fs} and use $\hat{\mathbf{n}}$ to denote the unit normal that points out of the averaging volume on S_{ss} and S_{ff} and out of the solid grains on S_{fs}. Consider the quantity

$$\nabla_{\bar{\mathbf{x}}} \cdot [(1-\eta)\bar{\boldsymbol{\sigma}}_s] = \frac{1}{V}\nabla_{\bar{\mathbf{x}}} \cdot \int_{V_s} \boldsymbol{\sigma}_s \, dV. \tag{26}$$

Physically, $\nabla_{\bar{\mathbf{x}}}$ describes the change in an averaged quantity due to an infinitesimal shift in the centroid $\bar{\mathbf{x}}$ of the averaging volume. Only the variation in the position of the boundary of V contributes to this change, hence

$$\nabla_{\bar{\mathbf{x}}} \cdot \int_{V_s} \boldsymbol{\sigma}_s \, dV = \int_{S_{ss}} \hat{\mathbf{n}} \cdot \boldsymbol{\sigma}_s \, dA. \tag{27}$$

By Gauss' theorem, the right side of Equation (27) can be written in the form

$$\int_{S_{ss}} \hat{\mathbf{n}} \cdot \boldsymbol{\sigma}_s \, dA = \int_{V_s} \nabla_{\mathbf{x}} \cdot \boldsymbol{\sigma}_s \, dV - \int_{S_{fs}} \hat{\mathbf{n}} \cdot \boldsymbol{\sigma}_s \, dA. \tag{28}$$

Thus, it follows that

$$\frac{1}{V} \int_{V_s} \nabla_{\mathbf{x}} \cdot \boldsymbol{\sigma}_s \, dV = \nabla_{\mathbf{x}} \cdot [(1-\eta)\bar{\boldsymbol{\sigma}}_s] + \frac{1}{V} \int_{S_{fs}} \hat{\mathbf{n}} \cdot \boldsymbol{\sigma}_s \, dA. \tag{29}$$

Equation (29), which relates the average of a divergence to the divergence of an average, is known as the Slattery-Whitaker averaging theorem. A similar result applies to the fluid stress, namely

$$\frac{1}{V} \int_{V_f} \nabla_{\mathbf{x}} \cdot \boldsymbol{\sigma}_f \, dA = -\nabla_{\bar{\mathbf{x}}}(\eta \bar{p}_f) - \frac{1}{V} \int_{S_{fs}} \hat{\mathbf{n}} \cdot \boldsymbol{\sigma}_f \, dA. \tag{30}$$

The sign in front of the surface integral over S_{fs} differs from that in Equation (29) because of the convention that $\hat{\mathbf{n}}$ points out of the solid grains into the pore spaces.

The final macroscopic solid and fluid equations, obtained by inserting Equations (29) and (30) into (24), are

$$\nabla_{\bar{\mathbf{x}}} \cdot [(1-\eta)\bar{\boldsymbol{\sigma}}_s] + (1-\eta)\bar{\rho}_s \mathbf{g} + \frac{1}{V} \int_{S_{fs}} \hat{\mathbf{n}} \cdot \boldsymbol{\sigma} \, dA = \mathbf{0}, \tag{31a}$$

$$-\nabla_{\mathbf{x}}(\eta \bar{p}_f) + \eta \rho_f \mathbf{g} - \frac{1}{V} \int_{S_{fs}} \hat{\mathbf{n}} \cdot \boldsymbol{\sigma} \, dA = \mathbf{0}. \tag{31b}$$

On the fluid-solid interface S_{fs} there is continuity of traction ($\hat{\mathbf{n}} \cdot \boldsymbol{\sigma}_s = \hat{\mathbf{n}} \cdot \boldsymbol{\sigma}_f$), so we have just written $\hat{\mathbf{n}} \cdot \boldsymbol{\sigma}$ in the surface integrals. By adding Equations (31) we obtain the simple result

$$\nabla_{\bar{\mathbf{x}}} \cdot \bar{\boldsymbol{\sigma}} + \bar{\rho}\mathbf{g} = \mathbf{0}. \tag{32}$$

The quantities

$$\bar{\boldsymbol{\sigma}} = (1-\eta)\boldsymbol{\sigma}_s - \eta \bar{p}_f \mathbf{I}, \tag{33a}$$

$$\bar{\rho} = (1-\eta)\bar{\rho}_s + \eta \rho_f, \tag{33b}$$

are the aggregate stress and density, respectively, of the fluid-filled porous medium; these macroscopic aggregate variables satisfy the same static equilibrium equation as the microscopic solid and fluid variables.

Force Exerted by the Fluid on the Solid

The quantity $\mathbf{F}(\bar{\mathbf{x}})$, defined by

$$\mathbf{F} = \frac{1}{V}\int_{S_{fs}} \hat{\mathbf{n}}\cdot\boldsymbol{\sigma}\,\mathrm{d}A, \tag{34}$$

appears explicitly as an additional apparent body force in the macroscopic solid balance equation (31a). Physically, $\mathbf{F}$ is the macroscopic force per unit volume exerted by the pore fluid on the solid matrix; the solid exerts an equal and opposite force on the fluid, and this appears in Equation (31b). It is straightforward to evaluate $\mathbf{F}$ if the fluid is in a hydrostatic rest state:

$$\mathbf{u} = \mathbf{0}, \tag{35a}$$

$$\boldsymbol{\sigma}_f = (p_0 + \rho_f \mathbf{g}\cdot\mathbf{x})\mathbf{I}, \tag{35b}$$

where p_0 is a constant reference pressure. By Gauss' theorem, we have

$$\begin{aligned}\mathbf{F}_{\mathrm{hydro}} &= -\frac{1}{V}\int_{V_f} \nabla_{\bar{\mathbf{x}}}\cdot\boldsymbol{\sigma}_f\,\mathrm{d}V + \frac{1}{V}\int_{S_{sf}} \hat{\mathbf{n}}\cdot\boldsymbol{\sigma}_f\,\mathrm{d}A \\ &= \frac{1}{V}\int_{V_f} \rho_f\mathbf{g}\,\mathrm{d}V + \frac{1}{V}\int_{S_{fs}} \hat{\mathbf{n}}\cdot\boldsymbol{\sigma}_f\,\mathrm{d}A \\ &= \eta\rho_f\mathbf{g} - \frac{1}{V}\int_{S_{sf}} \hat{\mathbf{n}}p_0\,\mathrm{d}A - \frac{1}{V}\int_{S_{fs}} \hat{\mathbf{n}}(\rho_f\mathbf{g}\cdot\mathbf{x})\,\mathrm{d}A.\end{aligned} \tag{36}$$

Upon evaluating the first surface integral in Equation (36) using the Slattery-Whitaker averaging theorem, we obtain

$$\frac{1}{V}\int_{S_{sf}} \hat{\mathbf{n}}p_0\,\mathrm{d}A = p_0\nabla_{\mathbf{x}}\left[\frac{1}{V}\int_{V_f}\mathrm{d}V\right] = p_0\nabla_{\mathbf{x}}\eta. \tag{37}$$

A similar manipulation of the second surface integral gives

$$\begin{aligned}\frac{1}{V}\int_{S_{fs}} \hat{\mathbf{n}}(\rho_f\mathbf{g}\cdot\mathbf{x})\,\mathrm{d}A &= \nabla_{\bar{\mathbf{x}}}\left[\frac{1}{V}\int_{V_f}\mathbf{x}\,\mathrm{d}V\right]\cdot\rho_f\mathbf{g} = \nabla_{\bar{\mathbf{x}}}(\eta\bar{\mathbf{x}})\cdot\rho_f\mathbf{g} \\ &= \eta(\rho_f\mathbf{g}) + (\rho_f\mathbf{g}\cdot\bar{\mathbf{x}})\nabla_{\bar{\mathbf{x}}}\eta,\end{aligned} \tag{38}$$

by definition of the centroid $\bar{\mathbf{x}}$. Combining Equations (36)–(38), we find that

$$\mathbf{F}_{\mathrm{hydro}} = -(p_0 + \rho_f\mathbf{g}\cdot\bar{\mathbf{x}})\nabla_{\mathbf{x}}\eta = -\bar{p}_f\nabla_{\bar{\mathbf{x}}}\eta. \tag{39}$$

A hydrostatic pore fluid thus exerts no net force on a constant-porosity solid; more generally, $\mathbf{F}_{\text{hydro}}$ is in the direction of decreasing porosity. The above analysis shows that there is no Archimedean buoyancy force $-(1-\eta)\rho_f \mathbf{g}$ on a constant-porosity solid; this point is obscured in the discussion of Hubbert & Rubey (1959) because they do not calculate the physically relevant quantity $\mathbf{F}_{\text{hydro}}$.

The macroscopic moment balance equation (31b) in the fluid can be rewritten in the form

$$\mathbf{F} - \mathbf{F}_{\text{hydro}} = -\eta(\nabla_{\bar{\mathbf{x}}} \bar{p}_f - \rho_f \mathbf{g}). \tag{40}$$

The quantity $-\eta(\nabla_{\bar{\mathbf{x}}} \bar{p}_f - \rho_f \mathbf{g})$ is thus the additional force per unit volume on the solid due to the motion of the fluid. It is customary to write this so-called seepage force in the form (Bear 1972, pp. 184–89)

$$\mathbf{F} - \mathbf{F}_{\text{hydro}} = \eta \nu \mathbf{K}^{-1} \cdot \bar{\mathbf{u}}, \tag{41}$$

where $\mathbf{K}(\bar{\mathbf{x}})$ is the permeability tensor, and $\mathbf{K} \cdot \mathbf{K}^{-1} = \mathbf{K}^{-1} \cdot \mathbf{K} = \mathbf{I}$. The quantity $\bar{\mathbf{u}}(\bar{\mathbf{x}})$ is the macroscopic fluid velocity or averaged fluid flux per unit area (note the division by V instead of V_f):

$$\bar{\mathbf{u}} = \frac{1}{V} \int_{V_f} \mathbf{u} \, dV. \tag{42}$$

Equation (41) is a constitutive relation governing the macroscopic flow; the linear relation between $\mathbf{F} - \mathbf{F}_{\text{hydro}}$ and $\bar{\mathbf{u}}$ is a consequence of the linearity of the Navier-Stokes equation (20), which governs the flow on the microscopic scale (Neumann 1977). Inserting Equation (41) into Equation (40) reduces the macroscopic fluid equation to

$$\bar{\mathbf{u}} = -\nu^{-1} \mathbf{K} \cdot (\nabla_{\bar{\mathbf{x}}} \bar{p}_f - \rho_f \mathbf{g}). \tag{43}$$

This is the usual form of Darcy's law (Batchelor 1967, pp. 223–24; Bear 1972, pp. 119–25).

Simplified Notation

Once the macroscopic equations have been derived, it is convenient to simplify the notation by dispensing with the subscripts on ∇ and the overbars used to denote averaged quantities. Accordingly, we rewrite Equation (43) in the form

$$\mathbf{u} = -\nu^{-1} \mathbf{K} \cdot (\nabla p_f - \rho_f \mathbf{g}). \tag{44}$$

Fluid flow within a noncompacting porous medium is determined by solving Equation (44) together with the macroscopic incompressibility condition $\nabla \cdot \mathbf{u} = 0$. In ground-water hydrology, it is common to

rewrite Equation (44) in the form $\mathbf{u} = -\nu^{-1}\rho_f g\mathbf{K}\cdot\nabla\Phi$, where $\Phi = (\rho_f g)^{-1}(p_f - \rho_f \mathbf{g}\cdot\mathbf{x})$ is the piezometric head (Bear 1972, pp. 122–23). The stress $\boldsymbol{\sigma}_s$ in the solid is related to that in the fluid by

$$\nabla\cdot[(1-\eta)\boldsymbol{\sigma}_s] + (1-\eta)\rho_s\mathbf{g} = \nabla(\eta p_f) - \eta\rho_f\mathbf{g}, \tag{45}$$

whereas the aggregate or porous medium stress $\boldsymbol{\sigma}$ satisfies

$$\nabla\cdot\boldsymbol{\sigma} + \rho\mathbf{g} = \mathbf{0}. \tag{46}$$

Equations (44)–(46) are valid at every point $\mathbf{x}$ in the macroscopic medium.

Effective Stress

The Coulomb failure criterion, which we consider next, depends on the effective stress in the porous medium, defined by

$$\boldsymbol{\sigma}^* = \boldsymbol{\sigma} + p_f\mathbf{I} = (1-\eta)(\boldsymbol{\sigma}_s + p_f\mathbf{I}). \tag{47}$$

Equations (44)–(46) are readily combined to yield

$$\nabla\cdot\boldsymbol{\sigma}^* + (1-\eta)(\rho_s - \rho_f)\mathbf{g} + \nu\mathbf{K}^{-1}\cdot\mathbf{u} = \mathbf{0}, \tag{48}$$

or, alternatively,

$$\nabla\cdot\boldsymbol{\sigma}^* + (1-\eta)\rho_s\mathbf{g} \quad (1 \quad \eta)\nabla p_f + \eta\nu\mathbf{K} \quad ^{1}\cdot\mathbf{u} = \mathbf{0}. \tag{49}$$

These equations involving the effective stress $\boldsymbol{\sigma}^*$ are commonly employed in soil mechanics and slope stability problems (e.g. Iverson & Major 1986). The second term $[(1-\eta)\rho_s\mathbf{g}]$ in Equation (49) is the gravitational attraction on the solid matrix, and the final term $[\eta\nu\mathbf{K}^{-1}\cdot\mathbf{u}]$ is the seepage force due to the motion of the fluid through the porous medium. The third term $[-(1-\eta)\nabla p_f]$ is frequently interpreted as an Archimedean buoyancy force acting on the solid matrix (Bear 1972, pp. 184–89), since that is what it reduces to if the fluid is in a hydrostatic rest state.

Discussion

In enumerating the body forces acting on a porous medium, it is necessary to distinguish which of the three stresses $\boldsymbol{\sigma}$, $\boldsymbol{\sigma}_s$, or $\boldsymbol{\sigma}^*$ is being considered—failure to do this was the cause of much of the controversy initiated by Hubbert & Rubey (1959). The aggregate stress $\boldsymbol{\sigma}$ satisfies Equation (46); the only body force in this case is the direct attraction of gravity on the porous medium, $\rho\mathbf{g}$. Equation (46) is valid even if the porosity is spatially variable and if there are nonhydrostatic pressure gradients causing fluid to percolate through the medium. If, instead, we wish to solve directly for the solid stress $\boldsymbol{\sigma}_s$, we must employ Equation (45). If the posority is uniform, (45) reduces to

$$\nabla \cdot \boldsymbol{\sigma}_s + \rho_s \mathbf{g} - \eta(1-\eta)^{-1}(\nabla p_f - \rho_f \mathbf{g}) = \mathbf{0}. \quad (50)$$

This has the same form as (46) if the pore-fluid pressure is hydrostatic; more generally, however, we must add $(1-\eta)^{-1}$ times the seepage force $\eta \nu \mathbf{K}^{-1} \cdot \mathbf{u}$. Finally, if we wish to solve directly for the effective stress $\boldsymbol{\sigma}^*$, we must employ Equation (49); in this case it is necessary to account for the Archimedean term $-(1-\eta)\nabla p_f$ as well as for the seepage force. Once any of the three stresses $\boldsymbol{\sigma}$, $\boldsymbol{\sigma}_s$, or $\boldsymbol{\sigma}^*$ has been determined, the others may be found subsequently; we are free to adopt the most convenient strategy.

COULOMB FAILURE CRITERION

There are a number of equivalent prescriptions of the Coulomb criterion; in reviewing these here, we account for cohesion as well as pore-fluid pressure. From a fundamental point of view, the strength of brittle materials is not well understood; in particular, there is no satisfactory explanation for the dependence on effective stress $\boldsymbol{\sigma}^*$. The Coulomb law is regarded here as a strictly empirical relation; laboratory data supporting its validity for rocks are reviewed by Jaeger & Cook (1969, pp. 136–82, 210–12) and Paterson (1978, pp. 16–50, 71–87). The effective stress principle was first stated for soils by Terzaghi (1923); a historical review is given by Skempton (1960).

Formulation in Terms of Principal Stresses

The right side of Figure 7 shows a sketch of an idealized laboratory rock mechanics fracture experiment. Three variables can be controlled independently: the applied axial stress σ_1, the confining stress σ_3, and the pore-fluid pressure p_f. The observed relationship between these three quantities at failure is

$$\sigma_1 + p_f = B(\sigma_3 + p_f) - C. \quad (51)$$

The constant B is related to the internal frictional angle ϕ by

$$B = \frac{1+\sin\phi}{1-\sin\phi}. \quad (52)$$

The constant C is called the uniaxial compressive strength.

The tractions exerted by the pistons and confining walls are transmitted to both the solid grains and the pore spaces, as shown in Figure 7 (*right*). The extent to which the fluid shares the load depends on the ratio A_f/A, where A is the total area of the boundary and A_f is the fraction of that area lying within the pore spaces. This so-called areal porosity is equal to the volumetric porosity η if the sample is homogeneous and isotropic.

With that proviso, the experimentally applied tractions may be interpreted as the macroscopic principal stresses in the porous aggregate:

$$\sigma_1 = (1-\eta)\sigma_{1s} - \eta p_f, \tag{53a}$$

$$\sigma_3 = (1-\eta)\sigma_{3s} - \eta p_f. \tag{53b}$$

The Coulomb law (51) can be rewritten in the form

$$\sigma_1^* = \left(\frac{1+\sin\phi}{1-\sin\phi}\right)\sigma_3^* - C, \tag{54}$$

where the quantities

$$\sigma_1^* = \sigma_1 + p_f = (1-\eta)(\sigma_{1s} + p_f), \tag{55a}$$

$$\sigma_3^* = \sigma_3 + p_f = (1-\eta)(\sigma_{3s} + p_f) \tag{55b}$$

are the effective principal stresses in the porous aggregate. With the sign convention adopted here, both σ_1^* and σ_3^* are negative in a typical experiment or in an active fold-and-thrust belt or accretionary wedge; failure occurs in the shaded region shown on the left in Figure 8.

Alternative Formulations

Let ψ be the counterclockwise angle from the x-axis to the local axis of greatest principal stress in a material, as shown in the center of Figure 8. Any two-dimensional state of stress can be written in the form

$$\sigma_{xx} = -p - R\cos 2\psi, \tag{56a}$$

$$\sigma_{zz} = -p + R\cos 2\psi, \tag{56b}$$

$$\sigma_{xz} = R\sin 2\psi, \tag{56c}$$

where

$$R = [\tfrac{1}{4}(\sigma_{zz} - \sigma_{xx})^2 + \sigma_{xz}^2]^{1/2}, \tag{57a}$$

$$p = -\tfrac{1}{2}(\sigma_{xx} + \sigma_{zz}). \tag{57b}$$

The quantity R is the radius of the Mohr circle, and p is called the mean aggregate stress. The aggregate principal stresses σ_1 and σ_3 are given in terms of p and R by

$$\sigma_1 = -p - R, \tag{58a}$$

$$\sigma_3 = -p + R. \tag{58b}$$

Alternatively, they may be written in terms of σ_{zz}, σ_{xx}, and ψ in the form

$$\sigma_1 = \sigma_{zz} - \tfrac{1}{2}(\sigma_{zz} - \sigma_{xx})(1 + \sec 2\psi), \tag{59a}$$

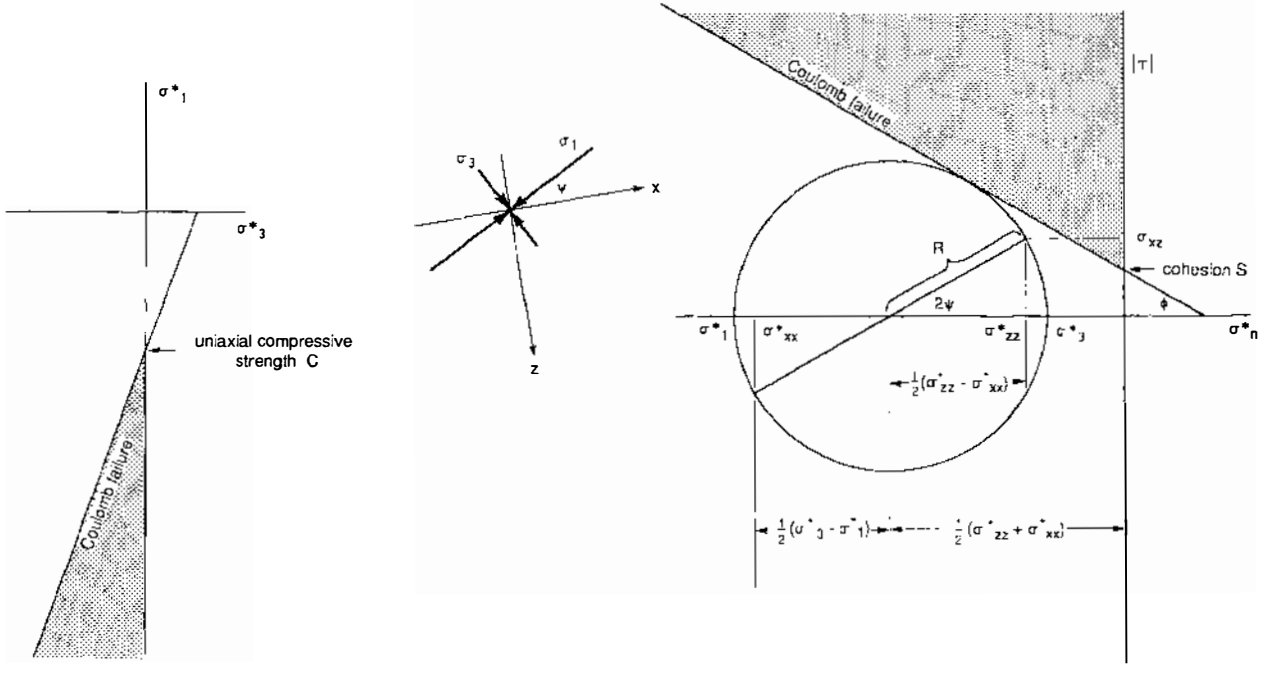

Figure 8 (*Left*) Relation between the effective principal stresses σ_1^* and σ_3^* in a noncohesive Coulomb material. (*Middle*) Orientation of the principal stresses σ_1 and σ_3 with respect to the coordinate axes x, z. (*Right*) Mohr diagram depicting the state of effective stress within a noncohesive Coulomb wedge.

$$\sigma_3 = \sigma_{zz} - \tfrac{1}{2}(\sigma_{zz} - \sigma_{xx})(1 - \sec 2\psi). \tag{59b}$$

The Coulomb criterion (54) can be written in terms of R, p, and p_f in the form

$$R = S\cos\phi + (p - p_f)\sin\phi = S\cos\phi + p^*\sin\phi. \tag{60}$$

The quantity S is the cohesion, given by

$$S = \tfrac{1}{2}C\left(\frac{1-\sin\phi}{\cos\phi}\right) = \tfrac{1}{2}C\left(\frac{1-\sin\phi}{1+\sin\phi}\right)^{1/2}. \tag{61}$$

Shear failure within an idealized Coulomb material occurs on conjugate surfaces oriented at angles $\pm\frac{1}{2}(90° - \phi)$ with respect to the axis of greatest principal stress σ_1. The shear traction $|\tau|$ on these planes is related to the effective normal traction $\sigma_n^* = \sigma_n + p_f = (1-\eta)(\sigma_{ns} + p_f)$ by

$$|\tau| = S - \mu\sigma_n^*, \tag{62}$$

where $\mu = \tan\phi$ is the coefficient of internal friction. The right side of Figure 8 shows a Mohr circle representation of the state of stress in a porous medium at failure. The quantities $\frac{1}{2}(\sigma_{zz} - \sigma_{xx}) = \frac{1}{2}(\sigma_{zz}^* - \sigma_{xx}^*)$ and $\sigma_{xz} = \sigma_{xz}^*$ can be written in terms of $\sigma_{zz}^* = \sigma_{zz} + p_f$ and ψ in the form

$$\tfrac{1}{2}(\sigma_{zz}^* - \sigma_{xx}^*) = \frac{S\cot\phi - \sigma_{zz}^*}{\csc\phi\sec 2\psi - 1}, \tag{63a}$$

$$\sigma_{xz}^* = \frac{\tan 2\psi\,[S\cot\phi - \sigma_{zz}^*]}{\csc\phi\sec 2\psi - 1}. \tag{63b}$$

Equations (63) are the most convenient form of the Coulomb failure criterion to use in the critical taper analysis that follows.

Noncohesive Approximation

Coefficients of internal friction measured in laboratory fracture experiments are in the range $\mu = 0.6$–1.0 for virtually all rocks; the corresponding internal friction angles are in the range $\phi = 30$–$45°$. Cohesion S varies much more widely, from nearly zero up to 150 MPa, with a strong dependence on porosity, cementation, mineralogy, and other factors. The shale and sandstone sedimentary rocks that are the predominant constituents of fold-and-thrust belts and accretionary wedges generally have $S = 5$–10 MPa (Hoshino et al 1972). Equations (62) and (63) show that such low values of cohesion are only important at shallow depths or where the pore-fluid pressure is very high; this suggests that a noncohesive critical taper model should be a reasonably good approximation for many geological applications. Equations (63) reduce, in the absence of cohesion, to

$$\tfrac{1}{2}(\sigma^*_{zz}-\sigma^*_{xx}) = \frac{-\sigma^*_{zz}}{\csc\phi\sec 2\psi - 1}, \tag{64a}$$

$$\sigma^*_{xz} = \frac{-\tan 2\psi\,\sigma^*_{zz}}{\csc\phi\sec 2\psi - 1}. \tag{64b}$$

It is noteworthy that these equations are satisfied by $\boldsymbol{\sigma}_s + p_f\mathbf{I}$ as well as by $\boldsymbol{\sigma}^*$, since a multiplicative factor of $1-\eta$ can be canceled on both sides.

Friction

Cohesion is also negligible in the case of frictional sliding on preexisting faults. Byerlee (1978) has shown that the laboratory coefficient of friction is remarkably uniform for a wide variety of rock types: $|\tau| = -0.85\sigma^*_n$ for $|\sigma^*_n| < 200$ MPa. Clay-rich fault gouges are characterized by lower coefficients, in the range 0.3–0.5 (Morrow et al 1981, Logan & Rauenzahn 1987).

NONCOHESIVE COULOMB WEDGE

Theory

Consider a submarine wedge with a planar upper surface, as shown in Figure 9; the results for a subaerial wedge can be recovered by setting the fluid density ρ_f equal to zero wherever it appears in a numbered equation below. We adopt a system of Cartesian coordinates, with x lying along the top of the wedge and z pointing obliquely down. Equation (46), the static equilibrium equation in terms of the aggregate stress $\boldsymbol{\sigma}$, becomes

$$\frac{\partial\sigma_{xx}}{\partial x} + \frac{\partial\sigma_{xz}}{\partial z} - \rho g z\sin\alpha = 0, \tag{65a}$$

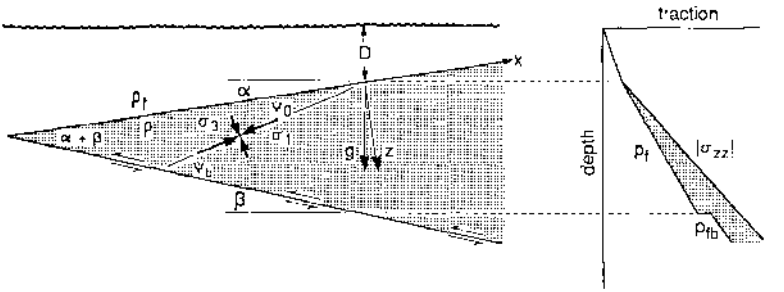

Figure 9 Idealized cross section of a submarine noncohesive critical wedge, showing the coordinate axes x, z and the angles α, β, ψ_0, and ψ_b. Strength in the wedge is proportional to the effective stress $\sigma^*_{zz} = \sigma_{zz} + p_f$, shown schematically by the shaded area on the right.

$$\frac{\partial \sigma_{xz}}{\partial x} + \frac{\partial \sigma_{zz}}{\partial z} + \rho g z \cos \alpha = 0. \tag{65b}$$

The boundary conditions on the upper surface of the wedge, $z = 0$, are

$$\sigma_{xz} = 0, \qquad \sigma_{zz} = -\rho_f g D, \tag{66}$$

where D is the water depth. It is convenient to define the generalized Hubbert & Rubey (1959) pore-fluid to lithostatic pressure ratio by

$$\lambda = \frac{p_f - \rho_f g D}{-\sigma_{zz} - \rho_f g D}. \tag{67}$$

We assume that λ, ρ, and the coefficient of internal friction μ are constant. Recall that ρ is the macroscopic density of the porous aggregate, given by $\rho = (1-\eta)\rho_s + \eta\rho_f$; if the wedge material is homogeneous, so that ρ_s is constant, then constancy of ρ implies constancy of the porosity η. Let ψ_0 be the angle between the x-axis and the axis of greatest principal stress σ_1, as shown in Figure 9. Equations (64)–(66) are then satisfied by

$$\sigma_{xz} = (\rho - \rho_f) g z \sin \alpha, \tag{68a}$$

$$\sigma_{zz} = -\rho_f g D - \rho g z \cos \alpha, \tag{68b}$$

$$\sigma_{xx} = -\rho_f g D - \rho g z \cos \alpha \begin{bmatrix} \csc \phi \sec 2\psi_0 - 2\lambda + 1 \\ \csc \phi \sec 2\psi_0 - 1 \end{bmatrix}, \tag{68c}$$

provided that

$$\frac{\tan 2\psi_0}{\csc \phi \sec 2\psi_0 - 1} = \left(\frac{1 - \rho_f/\rho}{1 - \lambda} \right) \tan \alpha. \tag{69}$$

Equation (69) relates the stress orientation angle ψ_0 to the surface slope α; we have assumed that ψ_0 is constant and have made use of the relation $dD/dx = -\sin \alpha$.

Equations (68) are an exact solution for the state of stress in a sloping half-space on the verge of Coulomb failure. All that remains is to satisfy the basal boundary condition. We allow for the possibility of a different pore-fluid regime on the décollement fault by writing the basal sliding condition in the form

$$\tau_b = -\mu_b(\sigma_n + p_{fb}). \tag{70}$$

The quantity p_{fb} is the pore-fluid pressure on the base, and μ_b is the basal coefficient of friction. Both μ_b and the basal pore-fluid to lithostatic pressure ratio defined by

$$\lambda_b = \frac{p_{fb} - \rho_f g D}{-\sigma_{zz} - \rho_f g D} \tag{71}$$

are assumed to be constant. In reality, the pore-fluid pressure cannot exhibit a jump discontinuity such as that shown in Figure 9, but the introduction of two constant Hubbert-Rubey ratios λ and λ_b provides a simple means of allowing for elevated pore-fluid pressures in the décollement zone. In order for a critical wedge to exist, its base must be a zone of weakness, i.e.

$$0 \leq \mu_b(1-\lambda_b) \leq \mu(1-\lambda). \tag{72}$$

The shear stress and normal stress on a surface whose dip is β are given as usual by (Malvern 1969, pp. 102–11)

$$\tau_b = \tfrac{1}{2}(\sigma_{zz} - \sigma_{xx}) \sin 2(\alpha+\beta) + \sigma_{xz} \cos 2(\alpha+\beta), \tag{73a}$$

$$\sigma_n = \sigma_{zz} - \sigma_{xz} \sin 2(\alpha+\beta) - \tfrac{1}{2}(\sigma_{zz} - \sigma_{xz})[1 - \cos 2(\alpha+\beta)]. \tag{73b}$$

Equations (68) and (73) are used to determine the dip of the surface on which the frictional sliding condition (70) is satisfied. We find, after some algebra, that β is given by

$$\alpha + \beta = \psi_b - \psi_0, \tag{74}$$

where

$$\frac{\tan 2\psi_b}{\csc \phi \sec 2\psi_b - 1} = \mu_b \left(\frac{1-\lambda_b}{1-\lambda} \right). \tag{75}$$

Equation (74) is the exact critical taper equation for a homogeneous noncohesive Coulomb wedge. It can be regarded as an equation of the form $\alpha + \beta = \psi_b - \psi_0(\alpha)$, which implicitly gives the surface slope α in terms of the basal dip β, the density ratio ρ_f/ρ, and the strength parameters μ, λ, μ_b, and λ_b. The quantity ψ_b is the angle between the axis of greatest principal stress σ_1 and the base of the wedge; thus, Equation (74) expresses an elementary relation between two internal angles and the opposite external angle of a triangle, as shown in Figure 9. Since the orientation of the principal stresses is everywhere the same, a noncohesive critical wedge is self-similar in the sense that a magnified version of any portion of it near the toe is indistinguishable from the wedge as a whole; this is a consequence of the absence of an inherent length scale in the equations of equilibrium and in the boundary and failure conditions. The exact critical taper equation involves only the angles α and β and the dimensionless parameters ρ_f/ρ, μ, λ, μ_b, and λ_b.

Equations (69) and (75) may be rewritten in the explicit form

$$\psi_0 = \tfrac{1}{2}\arcsin\left(\frac{\sin\alpha'}{\sin\phi}\right) - \tfrac{1}{2}\alpha', \tag{76a}$$

$$\psi_b = \tfrac{1}{2}\arcsin\left(\frac{\sin\phi'_b}{\sin\phi}\right) - \tfrac{1}{2}\phi'_b. \tag{76b}$$

The quantity α' is a modified surface slope angle defined by

$$\alpha' = \arctan\left[\left(\frac{1-\rho_f/\rho}{1-\lambda}\right)\tan\alpha\right], \tag{77}$$

and ϕ'_b is an effective basal friction angle defined by

$$\phi'_b = \arctan\left[\mu_b\left(\frac{1-\lambda_b}{1-\lambda}\right)\right]. \tag{78}$$

The multivalued nature of the arcsin functions in Equations (76) gives rise to a multiplicity of solutions with both compressional and extensional states of stress within the wedge and both possible orientations of the shear stress τ_b on the basal décollement fault (Dahlen 1984). The solution applicable to an active fold-and-thrust belt or accretionary wedge is obtained by choosing both ψ_0 and ψ_b to be positive acute angles, as shown in Figure 9. A different but equivalent form of the general solution (for the special case of a noncohesive dry subaerial wedge) dates back to Coulomb's (1773) analysis of the load exerted on a rough retaining wall. Dahlen (1984) was unaware of this venerable result and rediscovered it in the present context. A more systematic derivation, which exploits the observed scale invariance, is given by Barcilon (1987). Lehner (1986) has shown how the various multiple solutions can be obtained by a graphical construction method on the Mohr diagram.

Step-Up of Thrusts From the Basal Décollement Fault

Because of the self-similarity of a homogeneous noncohesive wedge, the failure surfaces oriented at $\pm\frac{1}{2}(90^\circ - \phi)$ with respect to the axis of greatest compressive stress σ_1 have the same dip everywhere. Forward-verging thrusts step up from the basal décollement fault at an angle

$$\delta_b = \tfrac{1}{2}(90^\circ - \phi) - \psi_b, \tag{79}$$

whereas the conjugate back-thrusts step up at a steeper angle

$$\delta'_b = \tfrac{1}{2}(90^\circ - \phi) + \psi_b. \tag{80}$$

The idealized geometry of these thrust faults and a Mohr diagram illustrating the basal state of effective stress in a noncohesive Coulomb wedge

are shown in Figure 10. The failure stress $|\tau|$ on both the forward and backward thrusts at the point where they step up into the wedge is given by

$$|\tau| = (\rho - \rho_f) gz \sin \alpha \left(\frac{\cos \phi}{\sin 2\psi_0} \right). \tag{81}$$

The frictional resistance on the basal décollement fault at the same point is

$$\tau_b = (\rho - \rho_f) gz \sin \alpha \left(\frac{\sin 2\psi_b}{\sin 2\psi_0} \right). \tag{82}$$

The quantity $\tau_b/|\tau| = \sin 2\psi_b/\cos \phi$ is a depth-independent measure of the ratio of décollement fault strength to wedge strength that must be in the range $0 \leq \tau_b/|\tau| \leq 1$ for every active fold-and-thrust belt or accretionary wedge. The quantity $\rho gz \sin \alpha$ has been employed in glaciology for at least 40 years to estimate the traction acting on the bed of a glacier (Orowan 1949). It has also been used by Elliott (1976) and others to estimate the traction at the base of a subaerial thrust sheet. For a noncohesive wedge on the verge of Coulomb failure everywhere, this glacial rule-of-thumb is biased low by a factor $\sin 2\psi_b/\sin 2\psi_0$, as shown by Equation (82).

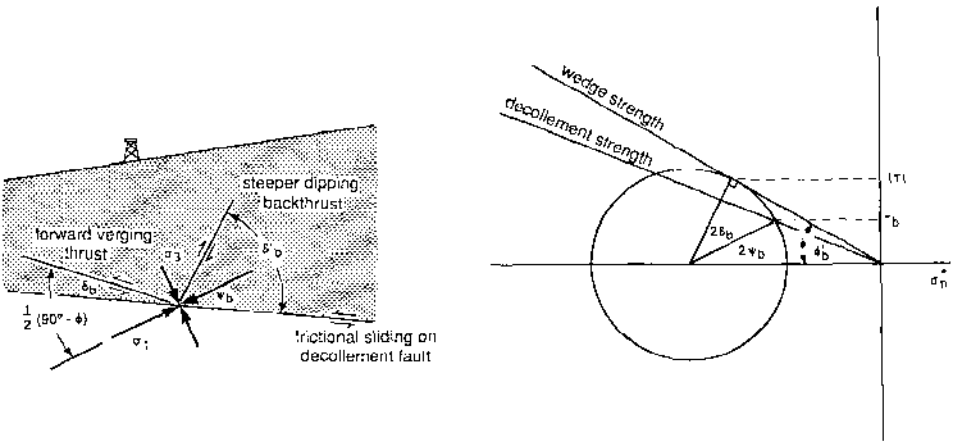

Figure 10 (*Left*) Geometry of self-similar thrust fault orientation within a critical noncohesive Coulomb wedge. Forward-verging thrusts exhibit a shallower dip due to the inclination between σ_1 and the base. (*Right*) Mohr diagram illustrating the basal state of effective stress.

Fluid Pressure Distribution and Fluid Flow

The pore-fluid pressure distribution within a noncohesive critical wedge is given by

$$p_f = \lambda \rho g z \cos\alpha. \tag{83}$$

In general, active fold-and-thrust belts and accretionary wedges are observed to be overpressured, i.e. the fluid-pressure ratio λ exceeds the hydrostatic value $\lambda_{hydro} = \rho_f/\rho$. Such elevated pore-fluid pressures will give rise to fluid flow within the wedge, and these percolating fluids will exert a seepage force on the solid wedge material, as discussed above. If the permeability of the wedge material is isotropic ($\mathbf{K} = k\mathbf{I}$), then the flow in a submarine wedge will be everywhere upward and normal to the upper surfaces:

$$\mathbf{u} = -\nu^{-1} k \rho g \cos\alpha (\lambda - \rho_f/\rho)\hat{\mathbf{z}} = \nu^{-1} k \rho g \cos\alpha (\lambda - \lambda_{hydro})\hat{\mathbf{z}}. \tag{84}$$

A subaerial fold-and-thrust belt has an additional small downslope component driven by the topography:

$$\mathbf{u} = -\nu^{-1} k \rho_f g \sin\alpha \hat{\mathbf{x}} - \nu^{-1} k \rho g \cos\alpha (\lambda - \lambda_{hydro})\hat{\mathbf{z}}. \tag{85}$$

In a steady-state wedge with a constant permeability k, the fluid flux $\mathbf{u}$ is pervasive and uniform. The source of the upward-flowing fluids is the dewatering of the sediments subducted beneath the wedge (Westbrook et al 1982, Moore 1989).

Small-Angle Approximation

The above results can be simplified by specializing to the case of a wedge having a narrow taper: $\alpha \ll 1$, $\beta \ll 1$, $\psi_0 \ll 1$, and $\psi_b \ll 1$. This should be a useful approximation for many thin-skinned fold-and-thrust belts and accretionary wedges. The simplifications arise from the replacement of sines and tangents of small angles by the angles themselves; cosines and secants are replaced by one to the same order of approximation. The specification $\psi_b \ll 1$ implies that the principal compressive stress σ_1 is quasi-horizontal; strictly speaking, this is only a valid approximation if the basal décollement fault is very weak [$\mu_b(1-\lambda_b) \ll \mu(1-\lambda)$].

The approximate critical taper equation takes the purely algebraic form

$$\alpha + \beta \approx \frac{(1-\rho_f/\rho)\beta + \mu_b(1-\lambda_b)}{(1-\rho_f/\rho) + 2(1-\lambda)\left(\dfrac{\sin\phi}{1-\sin\phi}\right)}. \tag{86}$$

This is the generalization of Equation (16) for a submarine wedge with pore-fluid pressure effects taken into account.

Laboratory Sandbox Models

Davis et al (1983) tested the predictions of the critical taper theory using an extremely simple laboratory model. Their apparatus consisted of a bottomless box containing well-sorted sand resting on a sheet of Mylar; the Mylar was supported by a flat rigid base whose dip was adjustable (Figure 11). The process of plate subduction was mimicked by slowly pulling the Mylar sheet beneath the sand; the frictional drag on the base induced deformation within the sand. Frictional drag on the transparent sidewalls was minimized by coating them with graphite before the sand was emplaced. The sand was stratified with passive black marker beds to allow the deformation within the wedge to be observed during an experimental run. Typically, the deformation was dominated by motion along a few discrete forward- and backward-verging thrust faults, as shown in Figure 12. The first faults formed near the rigid buttress at the back of the initially untapered wedge, and the locus of active faulting then moved toward the toe; deformation ceased once the critical taper was attained.

The loosely packed dry sand employed by Davis et al (1983) had a coefficient of internal friction $\mu \approx 0.6$ ($\phi \approx 30°$). The measured coefficient of friction between sand and Mylar was $\mu_b \approx 0.3$. The left side of Figure 13 compares the theoretical and observed critical tapers for four values of the basal dip β. Both the exact relationship between α and β and the small-angle approximation (16) are shown. Clearly, in this case, the small-angle approximation is valid; more importantly, the agreement of both the exact

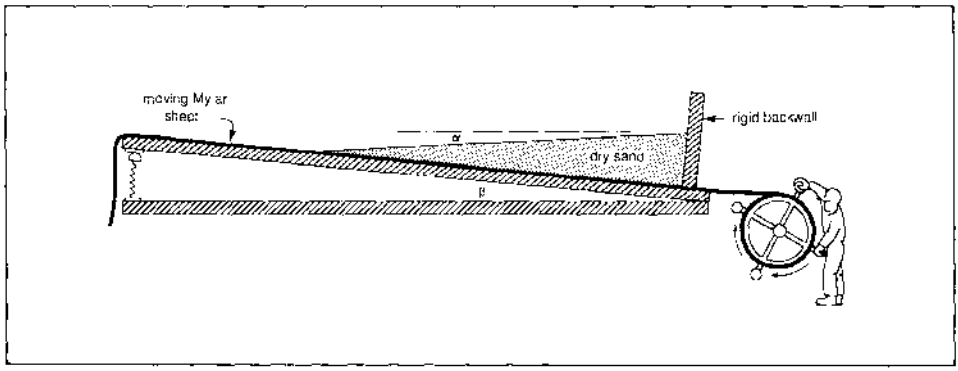

Figure 11 Schematic diagram of laboratory sandbox model. Actual length of rigid base is approximately 1 m. Figure in cap (Dan Davis) not shown to scale.

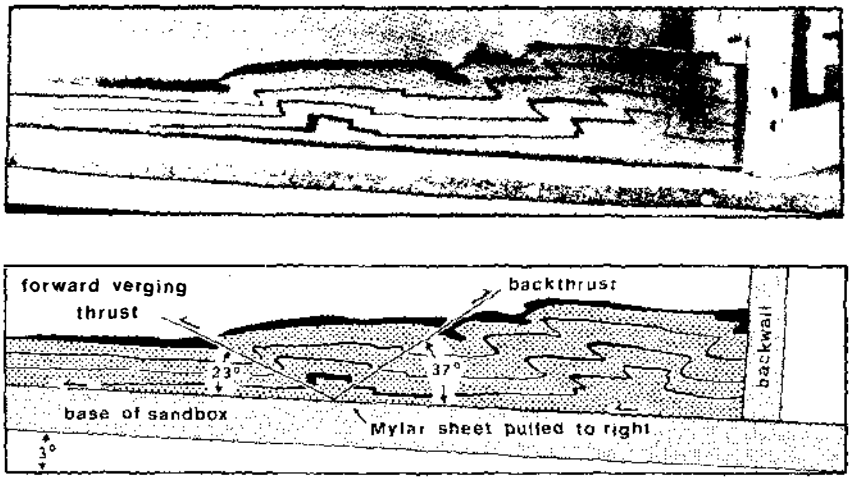

Figure 12 Photographic side view of a deforming sand wedge, showing discrete forward- and backward-verging thrust faults.

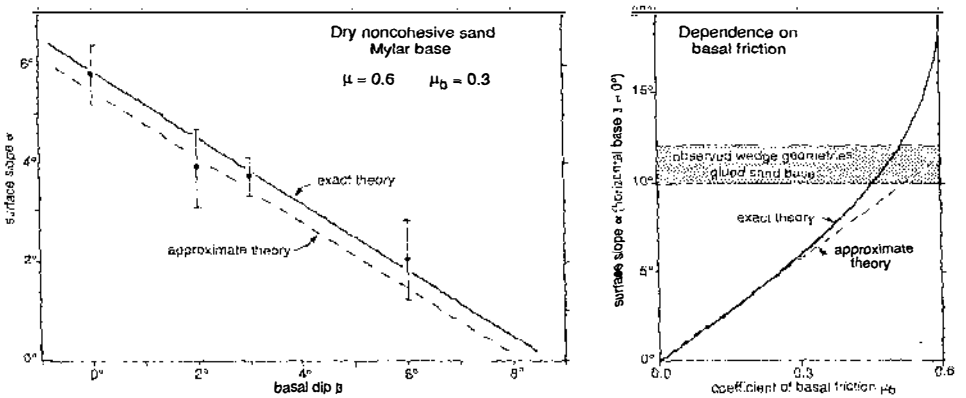

Figure 13 (*Left*) Comparison of theoretical critical surface slope with measured slopes in sandbox experiments (Davis et al 1983, Dahlen et al 1984). Dashed line is the small-angle approximation $\alpha = 5.7° - \frac{2}{3}\beta$. Dots represent the average of 8 experimental runs at $\beta = 0°$, 2 at $\beta = 2°$, 14 at $\beta = 3°$, and 9 at $\beta = 6°$. Bars denote the standard deviation. (*Right*) Theoretical dependence of α (for $\beta = 0°$) on the coefficient of basal friction μ_b. Dashed line is the small-angle approximation $\alpha = \frac{1}{3}\mu_b$.

and approximate results with the data is well within the experimental uncertainty. The observed basal step-up angles of the forward and backward thrust faults were compared with Equations (82) and (83) by Dahlen et al (1984). The angles were measured off photographs such as that in Figure 12; only freshly formed faults undistorted by subsequent faulting or rotation were included in the observations. The predicted step-up angles for $\mu = 0.6$, $\mu_b = 0.3$, and $\lambda = \lambda_b = 0$ are $\delta_b = 21°$ and $\delta_b' = 38°$. These agree very well with the observed values $\delta_b = 22 \pm 2°$ and $\delta_b' = 38 \pm 4°$.

To test the predicted dependence on the coefficient of basal friction μ_b, Goldberg (1982) conducted experimental runs using Mylar coated with sand as a base; the sand was glued to the Mylar base. The resulting surface slopes were significantly steeper than those produced on uncoated Mylar, in the range $\alpha = 10$–$12°$ compared with $\alpha = 5$–$7°$ for $\beta = 0°$. The right side of Figure 13 shows the predicted dependence on μ_b for $\mu = 0.6$ and $\lambda = \lambda_b = 0$. The increasing discrepancy between the exact results and the small-angle approximation as μ_b approaches μ is evident; the approximation is accurate to within 10% provided the basal friction is 10–15% less than the internal friction. Goldburg (1982) did not attempt to measure μ_b for a glued sand base directly; the observed wedge geometries suggest, however, that $\mu_b \approx 0.5$.

Mulugeta (1988) has recently performed more sophisticated modeling experiments using a motorized Plexiglass squeeze-box in a centrifuge. Experiments using sand with rounded grains gave results in good agreement with critical taper theory, but those using more angular sand did not. This was attributed to the greater degree of compaction of the angular sand; an alternative explanation might, however, be the extreme sensitivity of the taper to μ_b when $\mu_b \approx \mu$ (Figure 13).

GEOLOGICAL APPLICATIONS

Both the success of the critical taper model on the laboratory scale and the scale invariance of the noncohesive theory encourage applications to more complicated and less well-constrained geological situations. We apply the model here to the two end-member wedges illustrated in Figure 2.

Taiwan

The island of Taiwan is the site of an ongoing collision between the Luzon island arc situated on the Philippine Sea plate and the stable continental margin of China situated on the Eurasian plate. The divergence between the strike of the arc and the margin results in a southward-propagating collision that began about 4 Ma in the north and is occurring now at the southern tip of the island (Suppe 1981). Farther to the south, the oceanic

crust of the South China Sea is subducting beneath the Luzon arc along the Manila Trench, forming a submarine accretionary wedge on the east side of the trench. The subaerial fold-and-thrust belt that comprises more than half of the island of Taiwan forms by an expansion of this accretionary wedge as the arc encounters the thick sedimentary deposits on the Chinese continental slope and shelf. At the southernmost tip of the island, the mountains have just risen above sea level; to the north, the wedge grows in both height and width to become the Western Foothills, Hsuehshan Range, and Central Mountains of Taiwan.

This growth cannot continue unobstructedly because of the rapid tropical erosion. Between 23°N and 25°N latitude, the mountains exhibit a remarkably uniform surface slope and width $W = 90$ km. This morphology suggests strongly that the wedge has attained a dynamic steady state, with the accretionary influx balanced by the erosive efflux. The local rate of convergence between the Eurasian and Philippine Sea plates is $V = 70$ km Myr^{-1} (Seno 1977, Ranken et al 1984), and the thickness of the incoming sediments at the deformation front is estimated by drilling and seismic data to be $h = 7$ km (Suppe 1981). The average erosion rate, determined from both hydrological and geomorphological studies (Li 1976, Peng et al 1977), is $\dot{e} = 5.5$ km Myr^{-1}. The observed balance $hV = \dot{e}W$ confirms the steady-state nature of the deformation. North of 25°N, the mountains are being rifted on their eastern flank by the back-arc spreading in the Okinawa Trough; this major change in tectonic conditions is caused by the southward propagation of a reversal in the polarity of subduction as the Philippine Sea plate subducts beneath the Eurasian plate to the northeast of Taiwan (Suppe 1984).

Taiwan is an ideal natural laboratory for testing the validity of the critical taper model because of the abundant geophysical data acquired during petroleum exploration. The steady-state region is characterized by a regional surface slope $\alpha = 3°$ and a regional basal dip $\beta = 6°$ (Davis et al 1983). The basal dip is best determined in the front 30 km of the wedge by seismic reflection profiling, deep drilling, and the construction of retrodeformable cross sections (Suppe 1980). Pore-fluid pressures are also known in the front 30 km of the wedge from formation pressure tests and geophysical logging of numerous deep wells. The measured pore-fluid to lithostatic pressure ratio is $\lambda = \lambda_b = 0.67$ (Suppe & Wittke 1977, Davis et al 1983).

The critical taper model can be used to determine the range of basal and internal friction values consistent with the observed wedge geometry and pore-fluid pressures. The left side of Figure 14 shows the theoretical relation between α and β for various values of μ_b and μ. The geometry of the Taiwan wedge is consistent with the model, but the parameters cannot

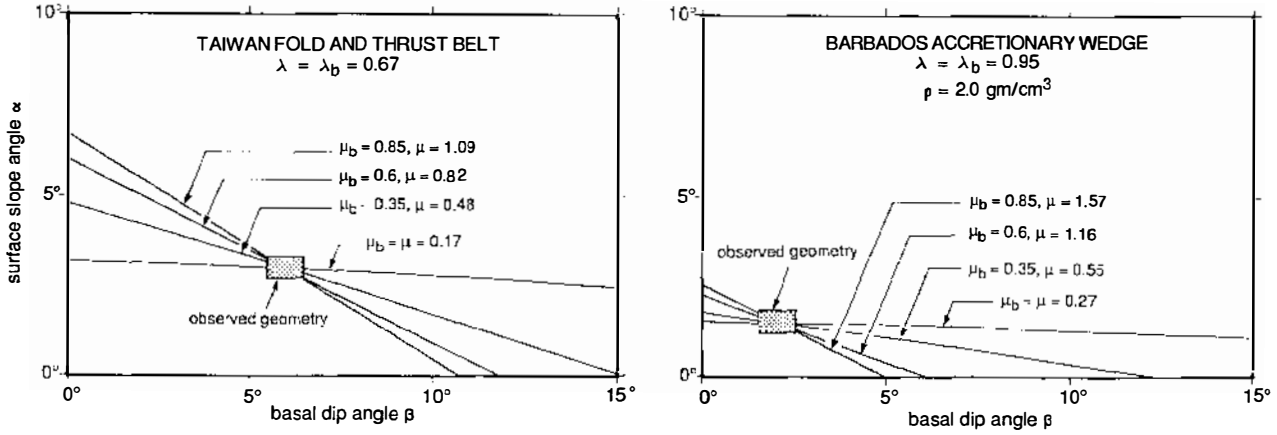

Figure 14 Theoretical surface slope α versus basal dip β for the Taiwan fold-and-thrust belt (*left*) and the Barbados accretionary wedge (*right*). Many possible combinations of μ_b and μ are consistent with the observed geometries and pore-fluid pressures.

be well constrained; the coefficient of friction μ_b on the décollement fault can be as low as 0.17 or in excess of 1. If μ_b is in the range of typical laboratory measurements for rocks and clay-rich fault gouges (0.3–0.85), then μ must exceed μ_b by 20–30%. This is an indication that the Taiwan wedge is not so pervasively fractured that frictional sliding is possible on surfaces of optimum orientation everywhere.

Barbados

The Barbados accretionary complex is located to the east of the Lesser Antilles island arc, where 65 Ma oceanic crust of the North American plate is subducting beneath the Caribbean plate (Westbrook 1975, 1982). The local rate of convergence between the two plates is $V = 2$ km Myr^{-1} (Minster & Jordan 1978, Sykes et al 1982). The thickness h of the incoming sediments varies by more than an order of magnitude, ranging from 7 km of mostly terrigenous sediments near the delta of the Orinoco River in the south to less than 1 km of hemipelagic muds in the north. The continuous accretion of these sediments since the Eocene has produced an accretionary prism of unusually great width ($\approx$300 km).

The geometry and internal structure of the Barbados wedge are particularly well known in the vicinity of 15°30′N latitude, where there has been a concentrated program of seismic reflection profiling and drilling (Westbrook et al 1982, 1989, Moore et al 1982, 1988). Only the uppermost two thirds of the thin incoming sediments in this region are being accreted at the deformation front; the underlying sediments are being underthrust beneath the toe, essentially undeformed (see Figure 2). The dip of the basal décollement fault is extremely shallow ($\beta = 2°$). The upper surface exhibits a slightly convex shape with a mean slope $\alpha = 1.5°$.

The entering sediments have initial porosities of 50–60%, but the porosity decreases both with depth and with distance to the deformation front as a result of compaction and dewatering (Bray & Karig 1985). If the average porosity for the wedge as a whole is $\eta = 30\%$, then the average value of the aggregate density of the porous medium is $\rho = 2000$ kg m^{-3}. Pore-fluid pressures are not nearly as well known in Barbados or any other accretionary wedge as they are in Taiwan. A single estimate obtained inadvertently at Deep Sea Drilling Project Site 542 during an attempt to free stuck drill string suggests that the pore-fluid to lithostatic pressure ratio near the deformation front is very high ($\lambda \approx \lambda_b \approx 0.9$–1). The ubiquitous presence of mud volcanic activity (Westbrook & Smith 1983) as well as the narrowness of the taper provide additional evidence for nearly lithostatic fluid pressures.

The right side of Figure 14 shows the theoretical relation between α and β for submarine wedges having $\rho = 2000$ kg m^{-3} and $\lambda = \lambda_b = 0.95$. As

in the case of Taiwan, the Barbados observations are consistent with the critical taper model, but they place very little constraint on the friction parameters μ_b and μ. The constraint that μ_b must be greater than 0.27 is not very robust because the pore-fluid pressure data are so circumstantial.

Heat Flow Constraint on Friction in Taiwan

An increase in μ_b increases the critical taper, whereas an increase in μ decreases it; this is the reason that the observed or estimated geometries and pore-fluid pressures in Taiwan and Barbados cannot constrain the level of friction. Twenty years ago, Brune et al (1969) pointed out that the level of frictional stress on the San Andreas fault could be determined by measuring the heat flow anomaly produced by frictional heating. Since that time, an extensive program of heat flow measurements has failed to reveal the expected narrow anomaly around the fault (Henyey & Wasserburg 1971, Lachenbruch & Sass 1973, 1980, 1988). In Taiwan, there is a substantial heat flow anomaly that can be attributed to brittle frictional heating; Barr & Dahlen (1989a,b) have used this anomaly to infer the effective coefficient of basal friction. A steady-state thermal model of the Taiwan fold-and-thrust belt was developed for this purpose; both shear heating on the décollement fault and internal strain heating within the deforming brittle wedge were incorporated in a mechanically consistent manner.

The left side of Figure 15 shows a contour map of the observed surface heat flow in Taiwan; the data were collected by Lee & Cheng (1986) from more than 100 oil wells, geothermal wells, and shallow boreholes. Prior to contouring, a robust smoother was applied to suppress spurious observations and enhance the regional pattern. In the steady-state region between 23°N and 25°N the smoothed contours are roughly parallel to the strike of the fold-and-thrust belt; the heat flow increases from its tectonically undisturbed value of 100 mW m^{-2} at the deformation front to more than 240 mW m^{-2} at the rear. The smoothed data between 23°N and 25°N are shown projected along strike on the right side of Figure 15. Theoretical heat flow curves for various values of the quantity $\mu_b(1-\lambda_b)$ are shown superimposed for comparison; in each case, the corresponding values of the wedge strength parameters μ and λ are chosen to be consistent with the observed Taiwan geometry. The heat flow data are best fit by $\mu_b(1-\lambda_b) = 0.16$. The effective coefficient of basal friction $\mu_b(1-\lambda_b)$ has been chosen as the fitting parameter rather than μ_b, since the basal pore-fluid ratio λ_b is only well determined in the vicinity of the deformation front. If the value measured there prevails along the entire décollement fault, the inferred coefficient of sliding friction is $\mu_b = 0.5$. This is lower than Byerlee's universal value of 0.85 for most rocks; it is, however, within the range of measured friction values for clay-rich fault gouges.

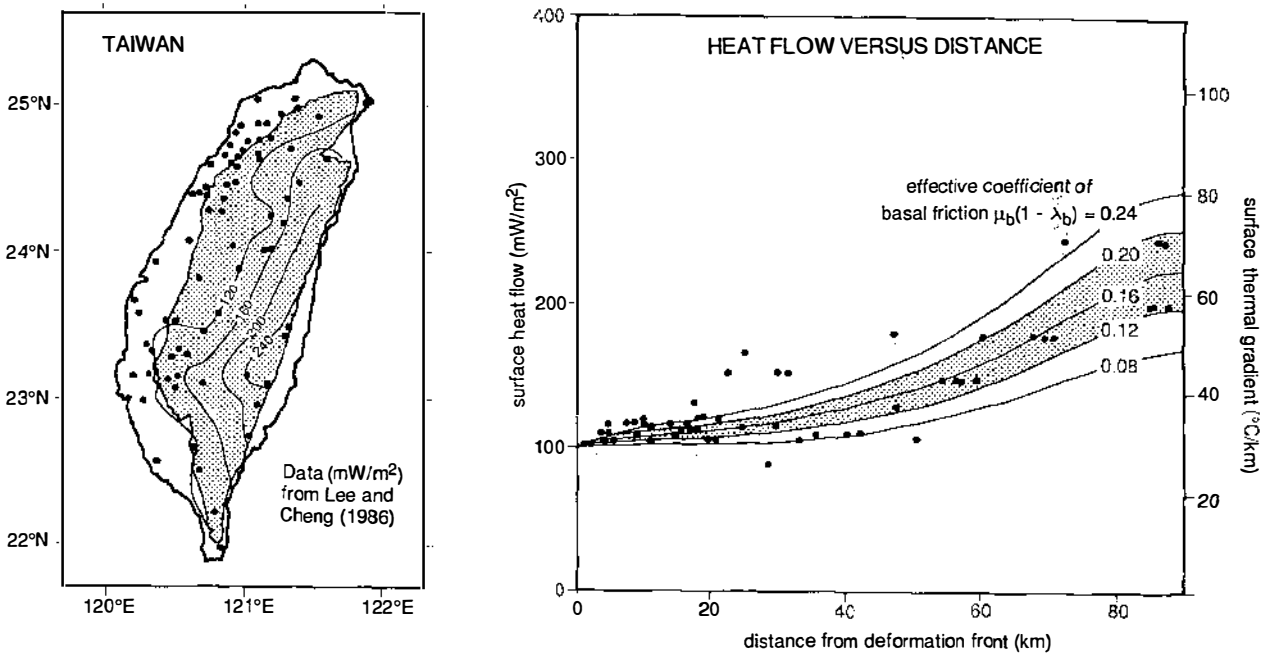

Figure 15 (*Left*) Smoothed surface heat flow on the island of Taiwan. (*Right*) Theoretical heat flow versus distance from the deformation front for various values of the effective coefficient of basal friction. Values in the shaded range $[\mu_b(1-\lambda_b) = 0.12\text{–}0.20]$ provide acceptable fits to the smoothed data (shown as dots).

APPROXIMATE GENERAL THEORY FOR A THIN-SKINNED WEDGE

The exact critical taper model described above is based on a number of extreme simplifying assumptions; in addition to ignoring cohesion, we have assumed that all the parameters ρ, λ, μ, λ_b, and μ_b are constant. Clearly, such simplifications are not realistic; on the other hand, there has been little motivation to develop a more general model in view of the almost complete lack of deep in situ measurements of pore-fluid pressure and other variables in active wedges. This situation is likely to change during the next decade as the geophysical exploration and characterization of active fold-and-thrust belts and accretionary wedges continue. Seismic data have already been used to infer the porosity distribution of two active wedges, Barbados (Westbrook et al 1989) and the Nankai Trough off southwestern Japan (Karig 1986). In this section, we extend the critical taper model to take into account spatial variations in porosity, pore-fluid pressure, and other parameters. For simplicity, we assume the principal stresses σ_1 and σ_3 are nearly horizontal and vertical, respectively, and consistently invoke small-angle approximations; the resulting theory for a thin-skinned wedge is quasi-analytical.

Theory

We consider a geometrically irregular submarine wedge, as shown in Figure 16; the case of a subaerial wedge can be recovered by setting the fluid density ρ_f equal to zero, as before. To begin with, we employ x- and z-axes that are locally aligned with the top of the wedge, as shown in the top sketch in Figure 16. The small-angle equations of static equilibrium within the wedge are then

$$\frac{\partial \sigma_{xx}}{\partial x} + \frac{\partial \sigma_{xz}}{\partial z} - \rho g \alpha \approx 0, \tag{87a}$$

$$\frac{\partial \sigma_{xz}}{\partial x} + \frac{\partial \sigma_{zz}}{\partial z} + \rho g \approx 0. \tag{87b}$$

The quantity $\partial \sigma_{xz}/\partial x$ can be ignored to first order in Equation (87b); the vertical (principal) stress due to the overlying water and porous wedge material is then found by integration to be

$$\sigma_{zz} \approx \sigma_3 \approx -\rho_f g D - g \int_0^z \rho \, dz. \tag{88}$$

The pore-fluid pressure p_f within the wedge is written in the form

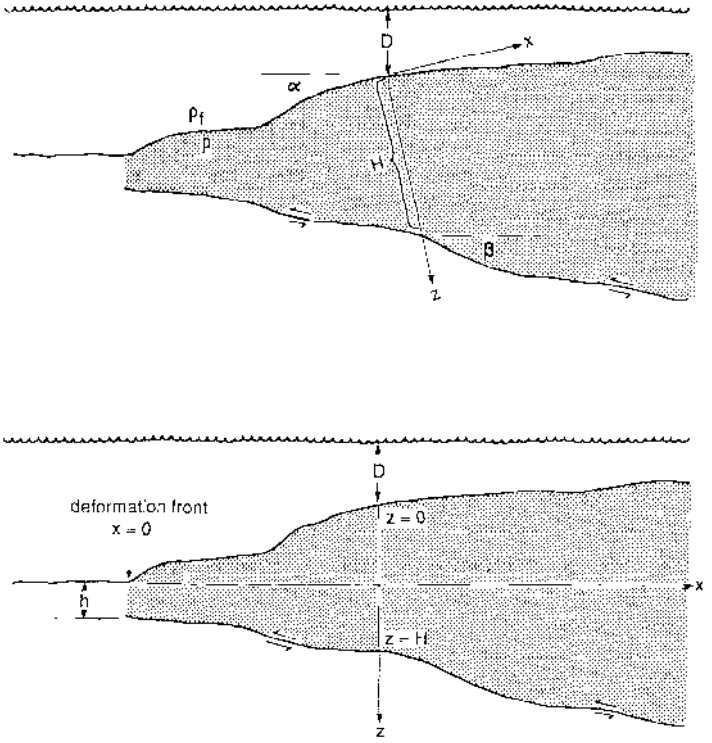

Figure 16 (*Top*) Schematic cross section of a geometrically irregular thin-skinned wedge with spatially variable mechanical properties. (*Bottom*) In applying the approximate critical taper equation (98), it is permissible to employ horizontal and vertical x- and z-axes.

$$p_f = \rho_f g D + \lambda g \int_0^z \rho \, dz. \tag{89}$$

Equation (89) simply serves to define the quantity λ; both λ and the aggregate density $\rho = (1-\eta)\rho_s + \eta\rho_f$ are regarded as functions of x and z within the wedge. In the small-angle approximation, it is also permissible to ignore the quantity σ_{xz}^2 in Equation (57a); the cohesive Coulomb failure criterion (60) thus takes the form

$$\tfrac{1}{2}(\sigma_{zz} - \sigma_{xx}) \approx S\cos\phi - \tfrac{1}{2}(\sigma_{xx} + \sigma_{zz} + 2p_f)\sin\phi. \tag{90}$$

Equation (90) can be solved for the horizontal (principal) stress:

$$\sigma_{xx} \approx \sigma_1 \approx -\rho_f g D - C - g\Lambda \int_0^z \rho \, dz, \tag{91}$$

where

$$\Lambda = 1+2(1-\lambda)\left(\frac{\sin\phi}{1-\sin\phi}\right). \tag{92}$$

The uniaxial compressive strength C and the angle of internal friction ϕ are also allowed to vary arbitrarily with position (x, z) inside the wedge.

The shear traction on the basal décollement fault, in the small-angle approximation, is

$$\tau_b \approx (\sigma_3-\sigma_1)(\alpha+\beta)+\sigma_{xz}. \tag{93}$$

To find σ_{xz} on $z = H$, we integrate Equation (87a); this gives

$$\sigma_{xz} \approx g\alpha\int_0^H(\rho-\rho_f)\,dz+\int_0^H(\partial C/\partial x)\,dz+g\int_0^H\frac{\partial}{\partial x}\left(\Lambda\int_0^z\rho\,dz\right)dz. \tag{94}$$

In writing Equation (94), we have used the fact that $dD/dx \approx -\alpha$. The final result for τ_b is most succinctly stated in terms of the depth-averaged quantities

$$\bar{\rho} = \frac{1}{H}\int_0^H\rho\,dz, \tag{95a}$$

$$\bar{C} = \frac{1}{H}\int_0^H C\,dz, \tag{95b}$$

$$\bar{\Gamma} - 2H^{-2}\int_0^H\Lambda\int_0^z\rho\,dz\,dz - 2H^{-2}\int_0^H\rho\int_0^z\Lambda\,dz\,dz. \tag{95c}$$

We find, after some reduction,

$$\tau_b \approx (\bar{\rho}-\rho_f)gH\alpha+\bar{C}(\alpha+\beta)+(\bar{\Gamma}-\bar{\rho})gH(\alpha+\beta) + H(d\bar{C}/dx)+\tfrac{1}{2}gH^2(d\bar{\Gamma}/dx). \tag{96}$$

The basal boundry condition requires that τ_b be equal to the coefficient of basal friction times the effective normal traction; we allow also for the possibility of a basal cohesion or plasticity S_b by writing

$$\tau_b \approx S_b+\mu_b(1-\lambda_b)\bar{\rho}gH. \tag{97}$$

Upon equating Equations (96) and (97), we obtain the approximate critical taper equation:

$$\alpha+\beta \approx \frac{[(1-\rho_f/\bar{\rho})\beta+\mu_b(1-\lambda_b)]\bar{\rho}gH+S_b-[d\bar{C}/dx+\frac{1}{2}gH(d\bar{\Gamma}/dx)]H}{(\bar{\Gamma}-\rho_f)gH+\bar{C}} \tag{98}$$

Once this result has been obtained, it is permissible to ignore the slight variable tilt of the x- and z-axes at different points in the wedge, as shown in Figure 16 (*bottom*). At every horizontal location x, we use Equations (95) to calculate the vertical averages $\bar{\rho}$, $\bar{C}$, and $\bar{\Gamma}$. The critical taper equation (98) then relates the local taper $\alpha+\beta$ to the local properties $\bar{\rho}$, $\bar{C}$, $\bar{\Gamma}$, S_b, $\mu_b(1-\lambda_b)$, and the local thickness H. The approximations that have been employed are valid as long as the base is relatively weak and the horizontal gradients in the properties are small. Since $\alpha+\beta \approx dH/dx$, we can regard Equation (98) as a first-order ordinary differential equation of the form $dH/dx \approx F(x,H)$. This equation can be integrated to find the wedge thickness $H(x)$, given the thickness $H(0)=h$ of the entering sediments at the deformation front $x=0$.

Special Cases

If all the properties are constant within the wedge, Equation (98) reduces to

$$\alpha+\beta \approx \frac{(1-\rho_f/\rho)\beta+\mu_b(1-\lambda_b)+S_b/\rho gH}{(1-\rho_f/\rho)+2(1-\lambda)\left(\dfrac{\sin\phi}{1-\sin\phi}\right)+C/\rho gH}. \tag{99}$$

This is the generalization of Equation (86) to a wedge with cohesion and basal plasticity. In the lithostatic limit $\lambda=\lambda_b=1$, Equation (99) becomes

$$\alpha+\beta \approx \frac{(1-\rho_f/\rho)\beta+S_b/\rho gH}{(1-\rho_f/\rho)+C/\rho gH}. \tag{100}$$

This is the small-angle solution for a perfectly plastic wedge obtained by Chapple (1978).

It is very common for pore-fluid pressures to be hydrostatic at shallow depths and overpressured at deeper depths. If cohesion and basal plasticity are ignored and both ρ and ϕ are assumed to be constant, Equation (98) reduces to

$$\alpha+\beta \approx \frac{(1-\rho_f/\rho)\beta+\mu_b(1-\lambda_b)+H\left(\dfrac{\sin\phi}{1-\sin\phi}\right)\left(\dfrac{d\bar{\lambda}}{dx}\right)}{(1-\rho_f/\rho)+2(1-\bar{\lambda})\left(\dfrac{\sin\phi}{1-\sin\phi}\right)}, \tag{101}$$

where

$$\bar{\lambda} = 2H^{-2}\int_0^H z\lambda\,\mathrm{d}z. \tag{102}$$

Equation (102) shows how vertical variations in the pore-fluid pressure ratio are averaged in such a way that the bottom of the column is more strongly weighted than the top; intuitively, it makes sense that the deeper portions of a wedge should be more important in determining the overall wedge strength.

To model the observed convexity of the Barbados wedge, Zhao et al (1986) considered a linear increase in cohesion with depth, $S = Kz$. Equation (98) reduces in this case to

$$\alpha+\beta \approx \frac{(1-\rho_f/\rho)+\mu_b(1-\bar{\lambda}_b)-\left(\frac{H}{\rho g}\frac{\mathrm{d}K}{\mathrm{d}x}\right)\left(\frac{\cos\phi}{1-\sin\phi}\right)}{(1-\rho_f/\rho)+\bar{\lambda}(1-\bar{\lambda})\left(\frac{\sin\phi}{1-\sin\phi}\right)+\left(\frac{K}{\rho g}\right)\left(\frac{\cos\phi}{1-\sin\phi}\right)}. \tag{103}$$

Equation (103) assumes that there is no basal plasticity and that all the wedge properties except the cohesion are constant. Zhao et al (1986) estimated the horizontal variation of K by a piecewise application of an exact critical taper model having $S = Kz$; such a procedure ignores the term involving the derivative $\mathrm{d}K/\mathrm{d}x$ in Equation (103). Fletcher (1989) derived Equation (103) and showed that the neglect of $\mathrm{d}K/\mathrm{d}x$ could lead to nonnegligible errors. Another defect of the Zhao et al (1986) analysis is their neglect of density variations; they treated ρ as constant in spite of the pronounced porosity variations.

Décollement Fault in Salt

Stresses in geological materials are limited by brittle fracture and frictional sliding at low temperatures, but by thermally activated processes (especially dislocation climb) at high temperatures (Brace & Kohlstedt 1980). Figure 17 illustrates the idealized dependence of typical rock strengths on depth; brittle frictional behavior is seen to prevail in the upper 10–15 km of the crust except in the case of evaporites, which flow plastically at substantially shallower depths. This extreme weakness of salt at upper crustal pressures and temperatures has an important effect on the mechanics of fold-and-thrust belts above salt, as noted by Davis & Engelder (1985).

The approximate critical taper of a fold-and-thrust belt whose décollement fault is in a salt horizon is given by Equation (99) with $\mu_b(1-\bar{\lambda}_b) = 0$. The depth-independent plastic strength of salt is $S_b \approx 1$ MPa; fold-and-thrust belts overlying salt have extremely narrow tapers ($\alpha+\beta \approx 1°$), since

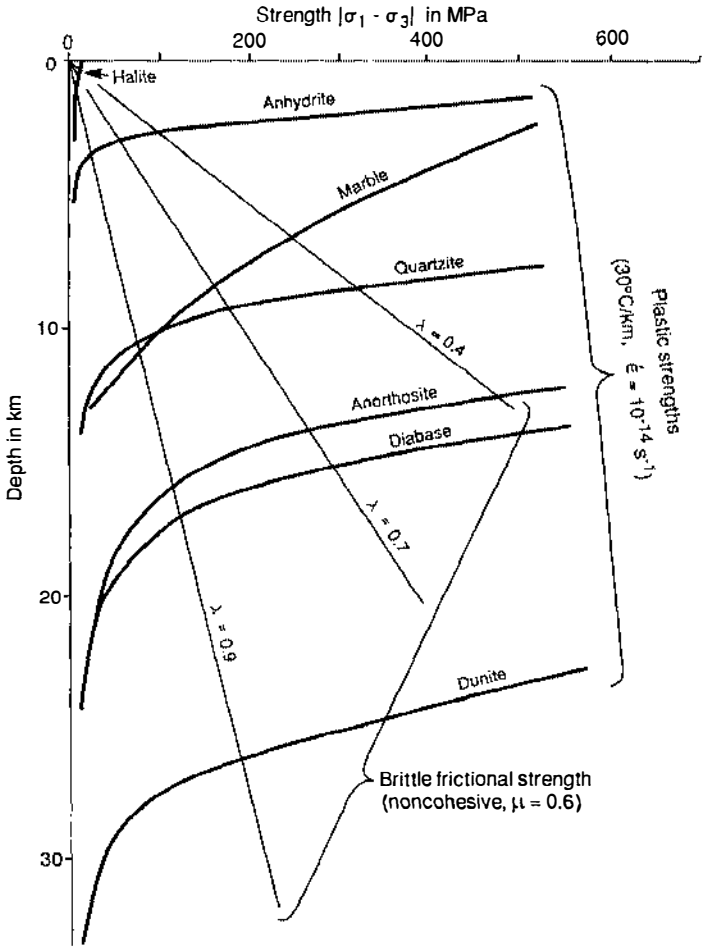

Figure 17 Idealized strength of rocks as a function of depth. Brittle frictional strength is largely independent of rock type, whereas plastic strengths vary considerably. This leads to a corresponding variation in depth to the brittle-plastic transition: 0–2 km for evaporites, 10–15 km for quartzofeldspathic rocks, and 25–30 km for olivine-rich rocks. Plastic strengths are extrapolated from laboratory data by assuming a typical geologic strain rate and geothermal gradient.

$S_b/\rho gH \ll 1$ if H is greater than a few kilometers. A cross section of the Zagros fold-and-thrust belt overlying the Hormuz salt in western Iran is shown in Figure 18; the extremely subdued topography is shown to true scale at the top.

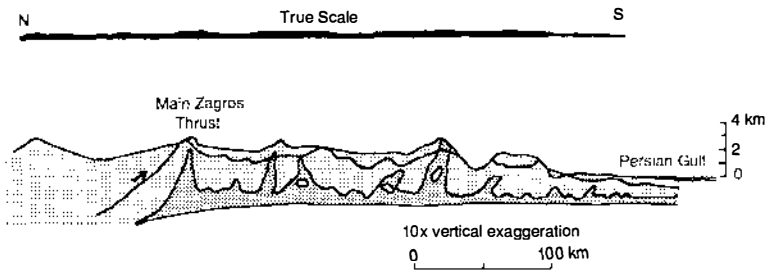

Figure 18 Cross section of the Zagros fold-and-thrust belt (Farhoudi 1978). Broad symmetrical anticlines are cored by diapiric salt, denoted by the dark stipple.

Forward-verging thrust faults generally predominate in fold-and-thrust belts not underlain by salt, since their shallower dip allows them to accommodate a greater amount of horizontal shortening than the steeper dipping back-thrusts for a given increase in gravitational potential energy. Salt-based fold-and-thrust belts, in contrast, generally lack a dominant sense of vergence; they are commonly characterized by broad, relatively symmetric folds (Davis & Engelder 1985). The theoretical step-up angles of forward- and backward-verging thrust faults are very nearly equal ($\delta'_b \approx \delta_b$) because the principal compressive stress σ_1 is almost parallel to the base (Figure 19). Simply stated, a fold-and-thrust belt riding on salt cannot tell from which direction it is being pushed.

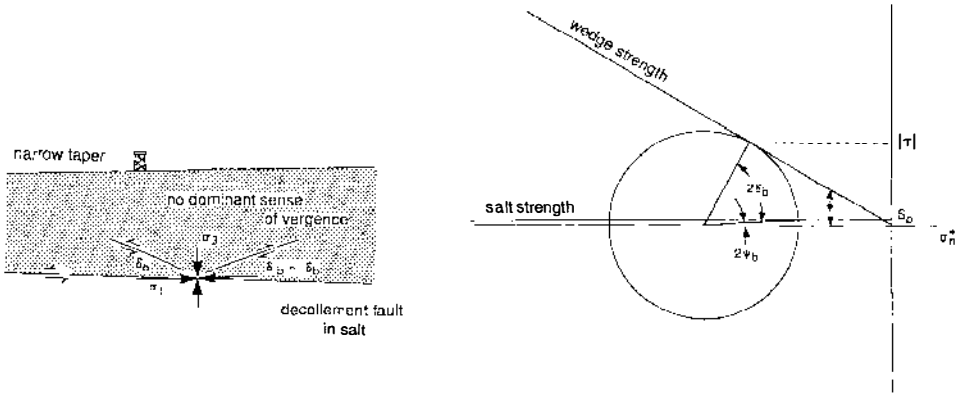

Figure 19 (*Left*) Schematic cross section illustrating the narrow taper and nearly symmetrical forward- and backward-verging thrust faults that characterize a fold-and-thrust belt overlying salt. (*Right*) Mohr diagram illustrating the basal state of effective stress. Compare with Figure 10.

Brittle-Plastic Transition

Basal plasticity can be important even in the absence of salt for wedges that have grown large enough to protrude beneath the brittle-plastic transition. Once this occurs, the shear traction on the basal décollement fault is abruptly decreased; the resulting reduction in the critical taper is again roughly described by Equation (99). A noneroding or slowly eroding wedge can only grow self-similarly if the drag on its base is purely frictional. It is thus the existence of a brittle-plastic transition at 10–15 km depth that ultimately limits the height of very wide fold-and-thrust belts and accretionary wedges. This provides a natural explanation for the break in topographic slope of the Higher Himalaya at the edge of the Tibetan Plateau (Figure 20).

CONCLUSION

The critical taper model is a useful paradigm for understanding the large-scale mechanics of fold-and-thrust belts and accretionary wedges. The theoretical formulation for a homogeneous noncohesive wedge is exact and entirely analytical. If one eschews elegance, the model can be generalized to take into account the spatial variation of mechanical properties and irregular geometries. The approximate general theory discussed here is limited to narrow tapers; exact, purely numerical models can, however, be developed using plastic slip-line theory (Hill 1950, pp. 128–60, 294–300; Stockmal 1983) or the finite element method. Hydrological models of pore-fluid pressures and flow rates in accretionary wedges have recently been developed (Shi & Wang 1988, Screaton et al 1989), and a logical next step would be to combine these with the critical taper model. The principal

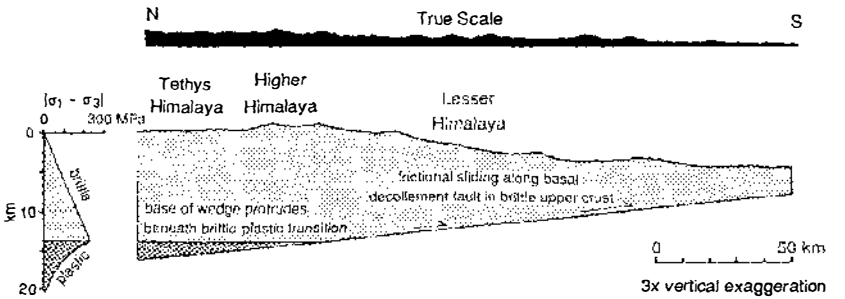

Figure 20 Schematic cross section of the Himalayan fold-and-thrust belt, showing the break in topographic slope in the Higher Himalaya at the edge of the Tibetan Plateau. A typical north-south topographic profile (along 82°30'E) is shown to true scale at the top.

obstacle at the present time is the meagerness of available data; the development of more detailed models must be preceded by the acquisition of structural, pore-fluid pressure, and heat flow data from active wedges.

ACKNOWLEDGMENTS

The critical Coulomb taper model has been developed in collaboration with Terence Barr, Dan Davis, John Suppe, and Wu-Ling Zhao. I thank Nancy Breen and Dan Orange for calling my attention to the seepage force and prompting me to think more carefully about the effect of pore fluids. Financial support has been provided by the National Science Foundation under grant EAR-8804098.

Literature Cited

Bally, A. W., Gordy, P. L., Stewart, G. A. 1966. Structure, seismic data and orogenic evolution of southern Canadian Rocky Mountains. *Bull. Can. Pet. Geol.* 14: 337–81

Barcilon, V. 1987. A note on "Noncohesive critical Coulomb wedges: An exact solution" by F. A. Dahlen. *J. Geophys. Res.* 92: 3681–82

Barr, T. D., Dahlen, F. A. 1989a. Brittle frictional mountain building. 2. Thermal structure and heat budget. *J. Geophys. Res.* 94: 3923–47

Barr, T. D., Dahlen, F. A. 1989b. Constraints on friction and stress in the Taiwan fold-and-thrust belt from heat flow and geochronology. *Geology*. In press

Batchelor, G. K. 1967. *An Introduction to Fluid Dynamics*. Cambridge: Univ. Press

Bear, J. 1972. *Dynamics of Fluids in Porous Media*. New York: Elsevier

Behrmann, J. H., Brown, K., Moore, J. C., Mascle, A., Taylor, E., et al. 1988. Evolution of structures and fabrics in the Barbados accretionary prism: insights from Leg 110 of the Ocean Drilling Program. *J. Struct. Geol.* 10: 577–91

Brace, W. F., Kohlstedt, D. L. 1980. Limits on lithospheric stress imposed by laboratory experiments. *J. Geophys. Res.* 85: 6248–52

Bray, C. J., Karig, D. E. 1985. Porosity of sediments in accretionary prisms and some implications for dewatering processes. *J. Geophys. Res.* 90: 768–78

Brune, J. N., Henyey, T. L., Roy, R. F. 1969. Heat flow, stress, and rate of slip along the San Andreas fault, California. *J. Geophys. Res.* 74: 3821–27

Byerlee, J. D. 1978. Friction of rocks. *Pure Appl. Geophys.* 92: 3681–82

Chapple, W. M. 1978. Mechanics of thin-skinned fold-and-thrust belts. *Geol. Soc. Am. Bull.* 89: 1189–98

Coulomb, C. A. 1773. Sur une application des règles de maximis et minimis à quelques problèmes de statique relatifs à l'architecture. *Acad. R. Sci. Mém. Math. Phys.* 7: 343–82

Dahlen, F. A. 1984. Noncohesive critical Coulomb wedges: an exact solution. *J. Geophys. Res.* 89: 10,125–33

Dahlen, F. A., Suppe, J., Davis, D. M. 1984. Mechanics of fold-and-thrust belts and accretionary wedges: cohesive Coulomb theory. *J. Geophys. Res.* 89: 10,087–10,101

Davis, D. M., Engelder, T. 1985. The role of salt in fold-and-thrust belts. *Tectonophysics* 119: 67–88

Davis, D., Suppe, J., Dahlen, F. A. 1983. Mechanics of fold-and-thrust belts and accretionary wedges. *J. Geophys. Res.* 88: 1153–72

Elliott, D. 1976. The motion of thrust sheets. *J. Geophys. Res.* 81: 949–63

Farhoudi, G. 1978. A comparison of Zagros geology to island arcs. *J. Geol.* 86: 323–34

Fletcher, R. C. 1989. Approximate analytical solutions for a cohesive fold-and-thrust wedge: some results for lateral variation in wedge properties and for finite wedge angle. *J. Geophys. Res.* 94: 10,347–54

Goldburg, B. 1982. *Formation of critical taper wedges by compression in a sandbox model*. BS thesis. Princeton Univ., Princeton, N.J. 70 pp.

Gray, W. G., O'Neill, K. 1976. On the general equations for flow in porous media and their reduction to Darcy's law. *Water Resour. Res.* 12: 148–54

Henyey, T. L., Wasserburg, G. J. 1971. Heat

flow near major strike-slip faults in California. *J. Geophys. Res.* 76: 7924–46

Hill, R. 1950. *The Mathematical Theory of Plasticity*. Oxford: Clarendon

Hoffman, P. F., Tirrul, R., King, J. E., St.-Onge, M. R., Lucas, S. B. 1988. Axial projections and modes of crustal thickening, eastern Wopmay orogen, northwest Canadian shield. In *Processes in Continental Lithospheric Deformation. Geol. Soc. Am. Spec. Pap.*, ed. S. P. Clark, B. C. Burchfiel, J. Suppe, 218: 1–29

Hoshino, K., Koide, H., Inami, K., Iwamura, S., Mitsui, S. 1972. Mechanical properties of Japanese Tertiary sedimentary rocks. *Rep. 244*, Geol. Surv. Jpn., Kawasaki. 200 pp.

Hubbert, M. K., Rubey, W. W. 1959. Role of fluid pressure in mechanics of overthrust faulting. 1. Mechanics of fluid-filled porous solids and its application to overthrust faulting. *Geol. Soc. Am. Bull.* 70: 115–66

Hubbert, M. K., Rubey, W. W. 1960. Role of fluid pressure in mechanics of overthrust faulting. Reply to discussion by H. P. Laubscher. *Geol. Soc. Am. Bull.* 71: 617–28

Hubbert, M. K., Rubey, W. W. 1961. Role of fluid pressure in mechanics of overthrust faulting. Reply to discussion by W. L. Moore. *Geol. Soc. Am. Bull.* 72: 1587–94

Iverson, R. M., Major, J. J. 1986. Groundwater seepage vectors and the potential for hillslope failure and debris flow mobilization. *Water Resour. Res.* 22: 1543–48

Jackson, J. D. 1962. *Classical Electrodynamics*. New York: Wiley

Jaeger, J. C., Cook, N. G. W. 1969. *Fundamentals of Rock Mechanics*. London: Methuen

Karig, D. E. 1986. Physical properties and mechanical state of accreted sediments in the Nankai Trough, S.W. Japan. In *Structural Fabrics in Deep Sea Drilling Project Cores From Forearcs. Geol. Soc. Am. Mem.*, ed. J. C. Moore. 166: 117–33

Lachenbruch, A. H., Sass, J. H. 1973. Thermo-mechanical aspects of the San Andreas fault system. *Proc. Conf. Tecton. Probl. of San Andreas Fault Syst.*, ed. R. L. Kovach, A. Nur, pp. 192–205. Stanford, Calif: Stanford Univ. Press

Lachenbruch, A. H., Sass, J. H. 1980. Heat flow and energetics of the San Andreas fault zone. *J. Geophys. Res.* 85: 6185–6223

Lachenbruch, A. H., Sass, J. H. 1988. The stress–heat flow paradox and thermal results from Cajon Pass. *Geophys. Res. Lett.* 15: 981–84

Laubscher, H. P. 1960. Role of fluid pressure in mechanics of overthrust faulting. *Geol. Soc. Am. Bull.* 71: 611–16

Lee, C. R., Cheng, W. T. 1986. *Preliminary heat flow measurements in Taiwan.* Presented at Circum-Pac. Energy and Miner. Resour. Conf., 4th, Singapore

Lehner, F. K. 1979. A derivation of the field equations for slow viscous flow through a porous medium. *Ind. Eng. Chem. Fundam.* 18: 41–45

Lehner, F. K. 1986. Comments on "Noncohesive critical Coulomb wedges: an exact solution" by F. A. Dahlen. *J. Geophys. Res.* 91: 793–96

Li, Y. H. 1976. Denudation of Taiwan island since the Pliocene epoch. *Geology* 4: 105 7

Logan, J. M., Raucnzahn, K. M. 1987. Frictional dependence of gouge mixtures of quartz and montmorillonite on velocity, composition and fabric. *Tectonophysics* 144: 87–108

Malvern, L. E. 1969. *Introduction to the Mechanics of a Continuous Medium.* Englewood Cliffs, NJ: Prentice-Hall

Minster, J. B., Jordan, T. H. 1978. Present-day plate motion. *J. Geophys. Res.* 83: 5331–54

Moore, J. C. 1989. Tectonics and hydrogeology of accretionary prisms: role of the décollement zone. *J. Struct. Geol.* 11: 95–106

Moore, J. C., Biju-Duval, B., Bergen, J. A., Blackington, B., Claypool, G. E., et al. 1982. Offscraping and underthrusting of sediment at the deformation front of the Barbados Ridge: Deep Sea Drilling Project Leg 78A. *Geol. Soc. Am. Bull.* 93: 1065–77

Moore, J. C., Mascle, A., Taylor, E., Andreieff, P., Alvarez, F., et al. 1988. Tectonics and hydrogeology of the northern Barbados Ridge: results from Leg 110 ODP. *Geol Soc. Am. Bull.* 100: 1578–93

Moore, W. L. 1961. Role of fluid pressure in overthrust faulting: a discussion. *Geol. Soc. Am. Bull.* 72: 1581–86

Morrow, C. A., Shi, L. Q., Byerlee, J. D. 1981. Permeability and strength of San Andreas fault gouge. *Geophys. Res. Lett.* 8: 325–28

Mulugeta, G. 1988. Modelling the geometry of Coulomb thrust wedges. *J. Struct. Geol.* 10: 847–59

Neumann, S. P. 1977. Theoretical derivation of Darcy's law. *Acta Mech.* 25: 153–70

Orowan, E. 1949. The flow of ice and other solids. *J. Glaciol.* 1: 231–40

Paterson, M. S. 1978. *Experimental Rock Deformation: The Brittle Field.* New York: Springer-Verlag

Peng, T. H., Li, Y. H., Wu, F. T. 1977. Tectonic uplift rates of the Taiwan island since the early Holocene. *Geol. Soc. China Mem.* 2: 57–69

Ranken, B., Cardwell, R. K., Karig, D. E. 1984. Kinematics of the Philippine Sea plate. *Tectonics* 3: 555–75

Roeder, D., Gilbert, O. E., Witherspoon, W. D. 1978. Evolution and macroscopic structure of Valley and Ridge thrust belt, Tennessee and Virginia. In *Studies in Geology 2*. Knoxville: Dept. Geol. Sci., Univ. Tenn. 25 pp.

Saffman, P. G. 1971. On the boundary condition at the surface of a porous medium. *Stud. Appl. Math.* 50: 93–101

Screaton, E. J., Wuthrich, D. R., Dreiss, S. J. 1989. Permeabilities, fluid pressures, and flow rates in the Barbados Ridge complex. *J. Geophys. Res.* In press

Seno, T. 1977. The instantaneous rotation vector of the Philippine Sea plate relative to the Eurasian plate. *Tectonophysics* 42: 209–26

Shi, Y., Wang, C. Y. 1988. Generation of high pore pressures in accretionary prisms: inferences from the Barbados subduction complex. *J. Geophys. Res.* 93: 8893–8909

Skempton, A. W. 1960. Terzaghi's discovery of effective stress. In *From Theory to Practice in Soil Mechanics: Selections from the Writings of Karl Terzaghi*, ed. L. Bjerrum, A. Casagrande, R. B. Peck, A. W. Skempton, pp. 42–53. New York: Wiley

Slattery, J. C. 1972. *Momentum, Energy, and Mass Transfer in Continua*. New York: McGraw-Hill

Stockmal, G. S. 1983. Modeling of large-scale accretionary wedge formation. *J. Geophys. Res.* 88: 8271–87

Suppe, J. 1980. A retrodeformable cross section of northern Taiwan. *Geol. Soc. China Proc.* 23: 46–55

Suppe, J. 1981. Mechanics of mountain building and metamorphism in Taiwan. *Geol. Soc. China Mem.* 4: 67–89

Suppe, J. 1984. Kinematics of arc-continent collision, flipping of subduction, and backarc spreading near Taiwan. *Geol. Soc. China Mem.* 6: 21–33

Suppe, J. 1987. The active Taiwan mountain belt. In *The Anatomy of Mountain Ranges*, ed. J. P. Schaer, J. Rodgers, pp. 277–93. Princeton, NJ: Princeton Univ. Press

Suppe, J., Wittke, J. H. 1977. Abnormal pore-fluid pressures in relation to stratigraphy and structure in the active fold-and-thrust belt of northwestern Taiwan. *Pet. Geol. Taiwan* 14: 11–24

Sykes, L. R., McCann, W. R., Kafka, A. L. 1982. Motion of Caribbean plate during last 7 million years and implications for earlier Cenozoic motions. *J. Geophys. Res.* 87: 10,656–76

Terzaghi, K. 1923. Die berechnung der durchlässigkeitsziffer des tones aus dem verlauf der hydrodynamischen spunnungserscheinungen. *Sitzungsber. Akad. Wiss. Wien* 132: 125–38

Westbrook, G. K. 1975. The structure of the crust and upper mantle in the region of Barbados and the Lesser Antilles. *Geophys. J. R. Astron. Soc.* 43: 201–42

Westbrook, G. K. 1982. The Barbados Ridge complex: tectonics of a mature forearc system. In *Trench-Forearc Geology: Sedimentation and Tectonics on Modern and Ancient Active Plate Margins*, ed. J. K. Leggett, pp. 275–90. London: Geol. Soc.

Westbrook, G. K., Ladd, J., Bangs, N. 1989. Structure of the northern Barbados accretionary prism. *Geology*. In press

Westbrook, G. K., Smith, M. J. 1983. Long décollements and mud volcanoes: evidence from the Barbados Ridge complex for the role of high pore-fluid pressure in the development of an accretionary complex. *Geology* 11: 279–83

Westbrook, G. K., Smith, M. J., Peacock, J. H., Poulter, M. J. 1982. Extensive underthrusting of undeformed sediment beneath the accretionary complex of the Lesser Antilles subduction zone. *Nature* 300: 625–28

Whitaker, S. 1969. Advances in theory of fluid motion in porous media. *Ind. Eng. Chem.* 61: 14–28

Zhao, W. L., Davis, D. M., Dahlen, F. A., Suppe, J. 1986. Origin of convex accretionary wedges: evidence from Barbados. *J. Geophys. Res.* 91: 10,246–58